UNIVERSIDADE ESTADUAL DE CAMPINAS

Faculdade de Engenharia Mecânica

ANDRES FELIPE RAMIREZ RODRIGUEZ

Laser surface alloying on Ti with Cr, Mo, and Cr-Mo, aiming to obtain a dissimilar Ti-Cr joint by additive manufacturing.

Titânio modificado superficialmente por laser com adições de Cr, Mo e Cr-Mo, visando a obtenção de uma junta Ti-Cr por manufatura aditiva.

Campinas

2023

ANDRES FELIPE RAMIREZ RODRIGUEZ

Laser surface alloying on Ti with Cr, Mo, and Cr-Mo, aiming to obtain a dissimilar Ti-Cr joint by additive manufacturing.

Titânio modificado superficialmente por laser com adições de Cr, Mo e Cr-Mo, visando a obtenção de uma junta Ti-Cr por manufatura aditiva.

Dissertation presented to the Faculty of Mechanical Engineer of the University of Campinas in partial fulfillment of the requirements for the degree of Master, in Mechanical Engineer the area of Materials and Manufacturing Process.

Dissertação apresentada à Faculdade de Engenharia Mecânica da Universidade Estadual de Campinas como parte dos requisitos exigidos para a obtenção do titulo de Mestre em Engenharia Mecânica na área de Materiais e Processos de Fabricação.

Orientador: Prof. Dr. João Batista Fogagnolo

ESTE EXEMPLAR CORRESPONDE À VERSÃO FINAL DA DISSERTAÇÃO DE MESTRADO DEFENDIDA PELO ALUNO ANDRES FELIPE RAMIREZ RODRIGUEZ, E ORIENTADA PELO PROF. DR. JOÃO BATISTA FOGAGNOLO.

.....
ASSINATURA DO ORIENTADOR

Campinas

2023

Ficha catalográfica
Universidade Estadual de Campinas
Biblioteca da Área de Engenharia e Arquitetura
Rose Meire da Silva - CRB 8/5974

R145L

Ramirez Rodriguez, Andres Felipe, 1987-
Laser surface alloying on Ti with Cr, Mo, and Cr-Mo, aiming to obtain a dissimilar Ti-Cr joint by additive manufacturing. / Andres Felipe Ramirez Rodriguez. – Campinas, SP : [s.n.], 2023.

Orientador: João Batista Fogagnolo.
Dissertação (mestrado) – Universidade Estadual de Campinas, Faculdade de Engenharia Mecânica.

1. Metais - Superfície. 2. Modificação de superfície. 3. Titânio. 4. Cromo. 5. Molibdênio. I. Fogagnolo, João Batista, 1964-. II. Universidade Estadual de Campinas. Faculdade de Engenharia Mecânica. III. Título.

Informações Complementares

Título em outro idioma: Titânio modificado superficialmente por laser com adições de Cr, Mo e Cr-Mo, visando a obtenção de uma junta Ti-Cr por manufatura aditiva.
Palavras-chave em inglês:
Metals - Surface
Surface modification
Titanium
Chromium
Molybdenum
Área de concentração: Materiais e Processos de Fabricação
Titulação: Mestre em Engenharia Mecânica
Banca examinadora:
João Batista Fogagnolo [Orientador]
Juliano Soyama
Conrado Ramos Moreira Afonso
Data de defesa: 30-06-2023
Programa de Pós-Graduação: Engenharia Mecânica

Identificação e informações acadêmicas do(a) aluno(a)
- ORCID do autor: https://orcid.org/0000-0002-5920-5137
- Currículo Lattes do autor: http://lattes.cnpq.br/2841154201936422

UNIVERSIDADE ESTADUAL DE CAMPINAS
FACULDADE DE ENGENHARIA MECÂNICA
COMISSÃO DE PÓS-GRADUAÇÃO EM ENGENHARIA MECÂNICA
DEPARTAMENTO DE ENGENHARIA DE MANUFATURA E MATERIAIS

DISSERTAÇÃO DE MESTRADO

Laser surface alloying on Ti with Cr, Mo, and Cr-Mo, aiming to obtain a dissimilar Ti-Cr joint by additive manufacturing.

Titânio modificado superficialmente por laser com adições de Cr, Mo e Cr-Mo, visando a obtenção de uma junta Ti-Cr por manufatura aditiva.

Autor: Andres Felipe Ramirez Rodriguez

Orientador: Prof. Dr. João Batista Fogagnolo

A Banca Examinadora composta pelos membros abaixo aprovou esta Dissertação de Mestrado:

Prof. Dr. João Batista Fogagnolo
DEMM/FEM/UNICAMP

Prof. Dr. Juliano Soyama
DEMM/FEM/UNICAMP

Prof. Dr. Conrado Ramos Moreira Afonso
DEMa/FEM/UFSCar

A Ata de Defesa com as respectivas assinaturas dos membros encontra-se no SIGA/Sistema de Fluxo de Dissertação/Tese e na Secretaria do Programa da Unidade.

Campinas, 30 de Junho de 2023

I dedicate this dissertation to my uncle Pedro Antonio and my aunt Concepcion, who now rests in peace.

Dedico esta disertación a mi tio Pedro Antonio y mi tia Concepcion, quienes ahora descansa en paz.

ACKNOWLEDGEMENTS

To God and my family for their love and affection, my mother, Rosa Elena, my brother Manuel, my grandmother Ana Beatriz and my aunt Martha.

To my MSc advisor: Professor Dr. Jõao Fogagnolo, for his unwavering support and friendship throughout this work.

To Professor Dr. Juliano Soyama for providing me with the chromium and molybdenum powders, materials essential for this work.

To my old friend Andres Galvis (Pola o q).

I also thank Angiee (Cuchu) for all the support.

To Professor Dr. Rubens Caram and his laboratory staff, Marcio, Leticia, and João, for the support.

I want to thank the technical staff of the multi-user laboratory, Marcia, Eduardo, and the didactic laboratory, Thiago and Saramago, for the technical support.

To my Lab friends Gueder and Sergio.

To my friends John (Navorski), Edgar, and Andrea.

To the University of Campinas for the opportunity to carry out this work.

This study was financed in part by the Coordenação de Aperfeiçoamento de Pessoal de Nível Superior - Brasil (CAPES) - Finance Code 001.

RESUMO

A manufatura aditiva é um conjunto de técnicas inovadoras que permitem, por exemplo, a fabricação de peças metálicas com alta precisão e geometrias complexas. No entanto, a maioria dos produtos metálicos fabricados por essas técnicas emprega apenas um metal ou liga metálica. A obtenção de juntas metálicas dissimilares por técnicas de manufatura aditiva é um campo que está começando a ser explorado para a fabricação de peças multimateriais, com gradientes de propriedades e funcionalidade para vários tipos de aplicações. Um dos obstáculos é a incompatibilidade entre elementos metálicos usados na fabricação dessas peças devida à formação de fases frágeis na interface, enfraquecendo a região da junta ou mesmo impedindo sua fabricação. Este trabalho estuda o processo de formação de ligas na superfície por laser para modificar a superfície de titânio comercialmente puro (Ti) com cromo (Cr), molibdênio (Mo) e Cr-Mo, usando Mo como material intermediário e obtendo uma junta Ti-Cr dissimilar por manufatura aditiva. Obtiveram-se cordões individuais de fusão superficial com adição de Mo e Cr sobre o Ti para a determinação dos parâmetros ideias para a produção de revestimentos contínuos de ambos os elementos. Variou-se a potência do laser de 150 a 450 W, mantendo-se a velocidade de varredura constante de 10 mm/s, uma distância da superfície da peça ao ponto focal do laser de 2 mm, correspondendo a um feixe com diâmetro de 254 μm, e uma altura de camada de 0,25 mm. A partir dos resultados dos cordões individuais de fusão superficial, determinaram-se as condições para a obtenção de uma e duas camadas contínuas pela sobreposição de 50% da largura dos cordões individuais, tanto para um revestimento de Cr quanto para um revestimento de Mo. Ao final, obtiveram-se a modificação superficial do titânio com a aplicação de uma camada de Mo e uma camada de Cr. Observaram-se, nos cordões individuais, o modo de condução para menores potências do laser e a transição para o modo keyhole com maior quantidade de poros para as maiores potências. A diluição aumentou com o aumento da potência do laser. Os cordões individuais modificados com Cr obtidos com baixa potência e os revestimentos com Cr apresentaram trincas, evidenciando a incompatibilidade entre o Ti e o Cr, enquanto a modificação superficial com Mo não apresentou trincas. A modificação superficial com camada contínua de Mo e Cr não apresentou as trincas, indicando que o uso do Mo pode viabilizar a obtenção de uma junta soldada entre Ti e Cr por manufatura aditiva.

Palavras–chave: Modificação superficial, Titânio, Cromo, Molibdênio, Manufatura aditiva

ABSTRACT

Additive manufacturing is a set of innovative techniques that allow, for example, manufacturing metal parts with high precision and complex geometries. However, most metal products these techniques manufacture use only one metal or metal alloy. Obtaining dissimilar metallic joints by additive manufacturing techniques is a field that is beginning to be explored for the manufacture of multi-compounds parts, with gradients of properties and functionality for various types of applications. One of the obstacles is the incompatibility between metallic elements used in manufacturing these parts due to the formation of brittle phases at the interface, weakening the joint region or even preventing its manufacture. This work uses laser surface alloying to modify the surface of commercially pure titanium (Ti) with chromium (Cr), molybdenum (Mo), and Cr-Mo, using Mo as intermediate material and obtaining a dissimilar Ti-Cr joint by additive manufacturing. Individual surface fusion strands were obtained with the addition of Mo and Cr on Ti to determine the optimal parameters for producing continuous coatings of both elements. The laser power was varied from 150 W to 450 W, with a constant scanning speed of 10 mm/s, a distance from the workpiece surface to the laser focal point of 2 mm, corresponding to a beam diameter of 254 μm, and a layer height of 0.25 mm. From the results of the individual strands of surface fusion, the conditions for obtaining one and two continuous layers were determined by overlapping 50% of the width of the individual strands for both a Cr coating and a Mo coating. Ultimately, titanium's surface modification was achieved by applying one Mo and one Cr layer. Conduction mode was observed in the individual strands for lower laser powers and transitioned to keyhole mode with more pores for the higher powers. The dilution increased with increasing laser power. The individual strands modified with Cr were obtained at low power, and the coatings with Cr showed cracks, evidencing the incompatibility between Ti and Cr. In contrast, the surface modification with Mo did not show cracks. The surface modification with a continuous layer of Mo and Cr did not present cracks, indicating that using Mo can make it feasible to obtain a welded joint between Ti and Cr by additive manufacturing.

Keywords: Surface Modification, Titanium, Chromium, Molybdenum, Additive Manufacturing.

LIST OF FIGURES

LIST OF TABLES

LIST OF ABBREVIATIONS AND ACRONYMS

HCP	Hexagonal Close Packed
BCC	Body Centered Cubic
FCC	Face Centered Cubic
Ti	Titanium
Ticp	Titanium commercially pure
Mo	Molybdenum
Cr	Chromium
SEM	Scanning Electron Microscopy
BSE	Backscattered Electrons
EDS	Energy Dispersive X-ray Spectroscopy
XRD	X-Ray Diffraction
μm	Micrometers
mm	Millimetres
mm/s	Millimetres per second
°C	Celsius degrees
W	Watts
R_X	Reflectivity coefficient
D_X	Volume density

CONTENTS

1 INTRODUCTION

Titanium (Ti) and its alloys are known to be some of the best engineering materials due to their excellent properties, including a high strength-to-weight ratio, which make them ideal for a wide range of applications (VEIGA *et al.*, 2012). To combine the advantageous mechanical and metallurgical properties of Ti with the availability or affordability of other alloys, there is a growing interest in modify Ti alloys with different super alloys (SZYMLEK, 2008) with high chromium (Cr) content as a common element, such as Inconel and Cobalt Chromium alloy, which also exhibit dissimilarity(SHANG *et al.*, 2020).

Unfortunately, the traditional titanium-chromium dissimilar joint has not been technically effective. Due to a metallurgical incompatibility between them, they generate intermetallic compounds like $\alpha TiCr_2$ and $TiCr_2$ which embrittle the surface and end up causing a collapse at the interface due to residual stress and excessive deformation generation(VOORT *et al.*, 2004).

Many authors have carried out studies to make viable by employing different techniques such as thermal fusion welding, friction stir welding, diffusion welding (GIRI *et al.*, 2022), and other techniques that are grouped within additive manufacturing, such as Direct Laser Deposition, Friction Stir Layer, Laser Welding, etc(REICHARDT *et al.*, 2021). The researchers searched for the right metal or alloy to use as intermediates to eliminate or alleviate the influence of intermetallic compounds at the interface, often based on binary phase diagrams(VOORT *et al.*, 2004) and aided by software simulation (ANDERSSON *et al.*, 2002), to get a sense of the outcome.

Surface modification on titanium is usually applied to change one or more of its most common properties: biocompatibility (CHOUIRFA *et al.*, 2019), osseointegration(JOHN *et al.*, 2016), corrosion resistance (SASIKUMAR *et al.*, 2019), and tribological resistance (KAUR *et al.*, 2019). However, surface modification is rarely seen to improve compatibility with other elements such as polymers (MOLITOR *et al.*, 2001), ceramics (CAI *et al.*, 2001), or even metals such as superalloys. The compatibility of Ti with other metals, whether pure or alloys (KAYSSER, 2001), is affected by the formation of intermetallic compounds, which change the physical and chemical properties of the substrate.

The formation of intermetallic compounds at the interface between dissimilar metals can significantly reduce the mechanical properties and reliability of the surface modification (PED-

DIRAJU *et al.*, 2020). One of the proposed solutions to avoid or minimize this issue is the use of intermediates that are compatible with both metals (substrate and dissimilar metal). In the case of joining titanium and chromium, the intermediates need to be compatible with both materials to avoid the formation of unwanted intermetallic compounds(LEE *et al.*, 2010).

To identify suitable intermediates for this research, the researchers consulted (LEVA, 2016; CARVALHO *et al.*, 2018; LI *et al.*, 2017) phase diagrams (VOORT *et al.*, 2004) and previous research on the topic (LI *et al.*, 2017). Phase diagrams provide important information on the behaviour of metals and their alloys at different temperatures and compositions. Based on this information, several candidates were proposed to carry out the research, taking into account their compatibility with both titanium and chromium(LI *et al.*, 2017).

Based on these investigations and the aforementioned phase diagrams, we proceeded to find metals that were compatible with Ti and Cr. Molybdenum (Mo)(LEVA, 2016) were found to be candidate for a first surface modification, avoiding the formation of intermetallic compounds between Ti and Cr by additive manufacturing. Using equipment own-design(LEVA, 2016), which allows the additive manufacturing powder bed fusion technique to be reproduced, an initial study of the compatibility between the metals was carried out, manufacturing single laser track at different laser powers, thus finding the compositions of the interfaces and preliminary results that allow us to report positive results in the viability of this joint.

1.1 Motivation and contribution

Materials science and engineering lies in the creation of novel materials with tailored properties to meet specific industrial needs. Recently, researchers have been particularly interested in dissimilar joints and multi-material alloy fabrication (REICHARDT *et al.*, 2021). These research areas have enormous potential for creating innovative solutions in industries such as aerospace and biomedical, where the demand for advanced materials with superior performance is constantly increasing.

The path of investigation of the dissimilar joint between Ti and Cr may also generate interesting data on the behavior of Ti in the presence of Cr treated by laser, varying the manufacturing power of the single laser track, obtaining also data on the dilution capacity of chromium in titanium and the direct dependence of this on the formation of the fusion zone. Additionally, previous results have shown that chromium concentration influences fractures and porosity in joints as it increases.

The study of the interface modification and dissimilar joint between Ti and Cr using Mo as an intermediate opens the door to generate new research in the union of dissimilar components and functional graded materials, such as the case of joining Ti with super alloys such as Inconel or GRX-810 (SMITH *et al.*, 2023) and Cobalt-Chromium, which is important in the nuclear, aerospace and medical industry, presenting a high content of Cr and Ni, which generate intermetallic compounds that embrittle the joint with Ti (CORIGLIANO; CRUPI, 2021). In the future, however, it may be possible to manufacture a wider range of study parts as test bodies by using intermediaries that are compatible with each other, allowing the joint's mechanical feasibility to be validated, as well as having multi-material parts and functional graded materials. In the same way, it is intended to contribute to additive manufacturing, relevant information for the manufacture of multicomponent parts, and indirectly, elements with gradient functionality.

1.2 Objectives

The main objective of this work is to obtain a laser surface modification between titanium and chromium using molybdenum as an intermediate material, using a own-design equipment to reproduce as many parameters as possible from the additive manufacturing powder bed fusion technique. Mechanical properties characterization will be carried out, including Vickers hardness and Young's modulus, in addition to X-ray diffraction and electron microscopy analysis to understand the microstructure characteristics.

To achieve this objective, the following strategy was employed:

(i) Single laser track of chromium and molybdenum powders were fabricated individually in Ti substrate, by varying the laser power available, taking into account previous data.

(ii) A sample with simple coating were fabricated to analyse the interface between the titanium sheets and each element separately (chromium and molybdenum).

(iii) Dual layer coating were fabricated to validate the interfaces and the variation of element concentration (chromium and molybdenum).

(iv) Based on these results, a laser surface alloying was made by initially using a layer of molybdenum and finally a layer of chromium.

As partial objectives, we can highlight: i) Evaluation of the compatibility between titanium and chromium at different laser powers. ii) Validation of the functionality of the own-

design equipment to reproduce the conditions generated in additive manufacturing. iii) Microstructural validation of the interface between titanium and the molybdenum-chromium mixture. iv) Evaluation of the concentration, and fusion zone dependence concerning on laser power.

2 THEORICAL PRINCIPLES

This chapter will summarize the principles on which the choice of Mo as an intermediate for the interface modification on Ti-Cr dissimilar joint is based; and other principles that were representative of the work.

2.1 Titanium and additive manufacturing

As the fourth most abundant metal in the earth's crust after aluminum, iron, and magnesium, titanium, located in period 4 and group IV, weighs 47.9 g/mol and has an atomic number 22, it is used in a wide variety of industries today, including aerospace, chemistry, sports, and biomedicine. It is found mainly in the minerals anatase, brookite, perovskite, rutile and tatanite. Having an incomplete 3d orbital, it enables titanium to form substitutional solid solutions with elements that present a difference in atomic size of approximately 20% (LIU *et al.*, 2004).

Furthermore, titanium is highly resistant to corrosion in aggressive environments, including organic acids, chlorine gas, and alkaline derivatives of these chemicals such as sodium hypochlorite; the oxide film that forms on its surface protects it from reacting with these compounds (DONACHIE, 2000).

In addition, Ti have become increasingly popular in the field of additive manufacturing due to their exceptional strength-to-weight ratio, corrosion resistance, and biocompatibility. The flexibility and precision of additive manufacturing techniques allow for the creation of complex geometries and customized designs that are difficult or impossible to achieve through traditional manufacturing methods (ZHANG *et al.*, 2018).

Additive manufacturing techniques as selective laser melting (SLM) and Powder bed fusion (PBF), have been particularly successful in the production of titanium components with high accuracy and density. These techniques involve the melting of titanium powder layer by layer, which allows for precise control over the shape, size, and orientation of the final product (ZHANG *et al.*, 2018).

The use of titanium in additive manufacturing has already led to significant advancements in various industries, including aerospace, automotive, medical, and sports equipment. For example, aerospace companies are using additive manufacturing to produce lightweight titanium components for jet engines and other critical aircraft parts (LI *et al.*, 2017; SMITH *et al.*, 2023).

Medical device manufacturers are also using additive manufacturing to produce customized implants and prosthetics that are biocompatible and can be tailored to each patient's unique needs (AGAPOVICHEV *et al.*, 2018).

Despite the numerous advantages of using titanium in additive manufacturing, challenges still exist in terms of material cost, process repeatability, and compatibility with other metals and alloys.

2.2 Compatibility between Ti and Cr

In recent years, there has been an increasing interest within the scientific community in studying the compatibility between titanium alloys and Cobalt-Chromium-based, and superalloys. These superalloys are commonly used in biomedical applications, such as dental implants and joint replacements, due to their excellent mechanical properties, corrosion resistance, and biocompatibility.

Another alloy that shows little or no compatibility with titanium is the Nickel-Chromium-based superalloys (SMITH *et al.*, 2023; ONUIKE; BANDYOPADHYAY, 2018; SHANG *et al.*, 2020), where the two main elements of this alloy are nickel and chromium, the latter of which is of interest for this work. Research on the compatibility of these two alloys shows results where there is delamination (ONUIKE; BANDYOPADHYAY, 2018), fracture, and low strength in the interface zone, due to the formation of intermetallic compounds with nickel and chromium, such as $\alpha TiCr_2$ (KURODA *et al.*, 2016) and $\beta TiCr_2$ (MOHAN *et al.*, 2021; ONUIKE; BANDYOPADHYAY, 2018). These intermetallic compounds, in combination with others, generate residual stresses that ultimately lead to material failure.

The figure 2.1 illustrates the phase diagram between titanium and chromium, showing intermetallic compounds forming in the entire concentration region.

The titanium-chromium system is a binary system that exhibits various intermetallic phases. The phase diagram of the system shows the different phases that can form as a function of temperature and composition. At low temperatures, the system is primarily composed of the HCP (hexagonal close-packed) alpha phase of titanium and the BCC (body-centered cubic) beta phase of chromium (MURRAY, 1981a).

As the temperature increases, the alpha phase of titanium transforms into the BCC beta phase, and the beta phase of chromium transforms into the FCC (face-centered cubic) gamma phase. At high temperatures, the system is primarily composed of the beta phase of both tita-

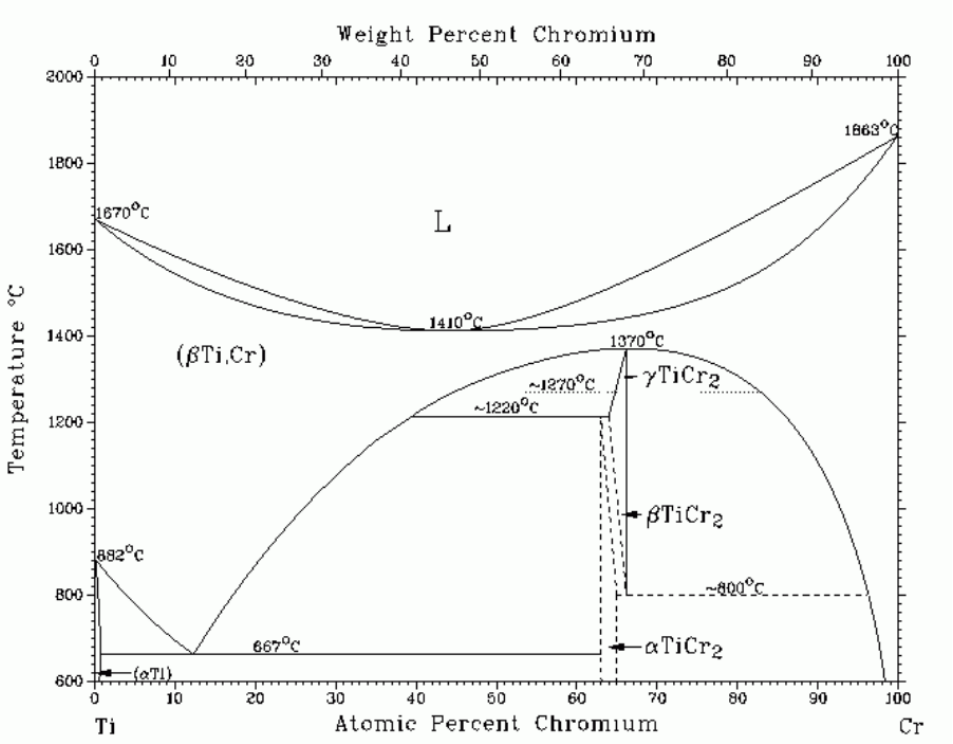

Figure 2.1 – Phase diagram Ti and Cr (MURRAY, 1981a).

nium and chromium (MURRAY, 1981a).

At certain compositions and temperatures, intermetallic compounds can form in the titanium-chromium system. The most notable of these compounds are the TiCr and $TiCr_2$ phases, which have been found to form in the system at specific compositions and temperatures. These phases can have a significant impact on the properties of materials that are composed of these two elements, including their mechanical properties, corrosion resistance, and biocompatibility (FOX *et al.*, 2008).

2.3 Ti and Mo system

The equilibrium phase diagram of the Ti-Mo binary system is depicted in Figure 2.2.

This phase diagram belongs to the isomorphic type, and at low temperatures, it exhibits three well defined regions: 1) a narrow α phase stability field for extremely low Mo contents; 2) a stability field of the mixture of α and β phases, which has a smaller range of compositions; 3) the stability field of the β phase for high Mo contents. With the increase in temperature, the α and $\alpha + \beta$ fields diminish in size, while the β field expands. Above 882 °C, the β phase becomes the only stable phase, and Mo displays complete solubility in the β phase across the entire range of compositions. The onset temperatures of solid/liquid transformations increase as

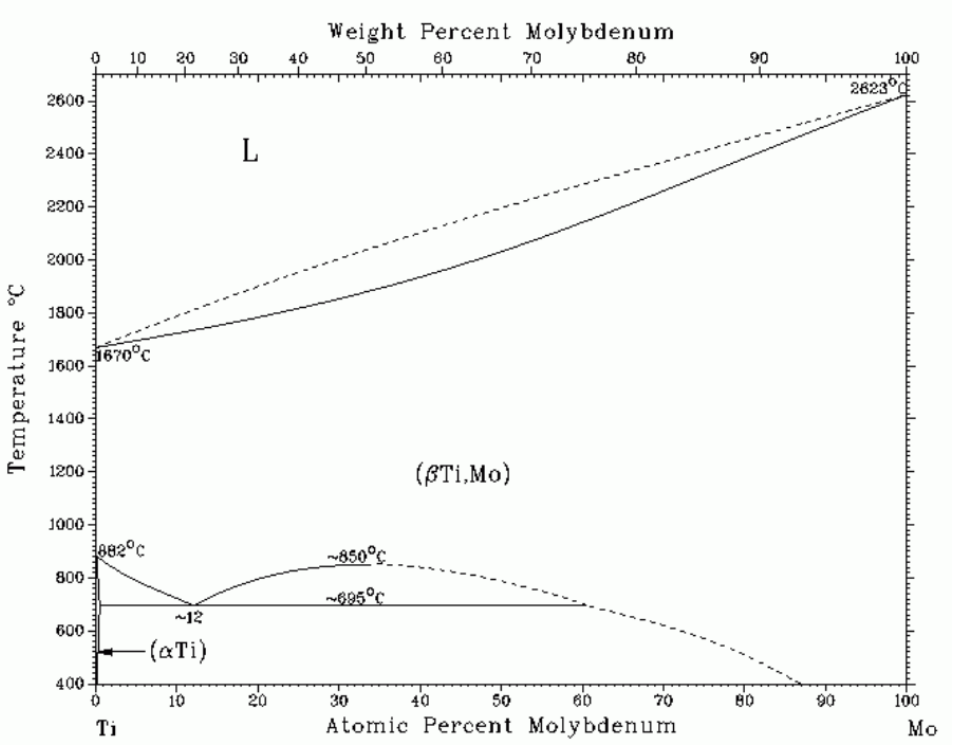

Figure 2.2 – Phase diagram Ti and Mo (MURRAY, 1981b).

the Mo content increases. The smallest value is 1670 °C, which is the melting point of titanium, and the maximum value is reached at 2625 °C, the melting point of Mo (MURRAY, 1981b).

2.4 Compatibility Mo and Cr

Another important phase diagram for the selection of Mo as an intermediate material is shown in Figure 2.3. This molybdenum-chromium system shows that these two elements form a solid solution with a body-centred cubic (BCC) structure at all weight percentages (VOORT *et al.*, 2004), without any intermetallic compounds.

However, there is a concentration gap in the phase diagram below 880 °C, which means that there can be non-combination of the two elements in certain concentrations and temperatures. This concentration gap is because a low diffusion rates involved, which affects the solubility and can lead to phase separation. Overall, the phase diagram of the Mo-Cr system indicates a high potential for compatibility as an intermediate material in dissimilar joints with titanium, as both elements exhibit a BCC structure and complete solid solubility (VENKATRAMAN; NEUMANN, 1987).

Unfortunately, the elemental system of Chromium and Molybdenum has not been extensively studied in the context of additive manufacturing. However, both elements have been

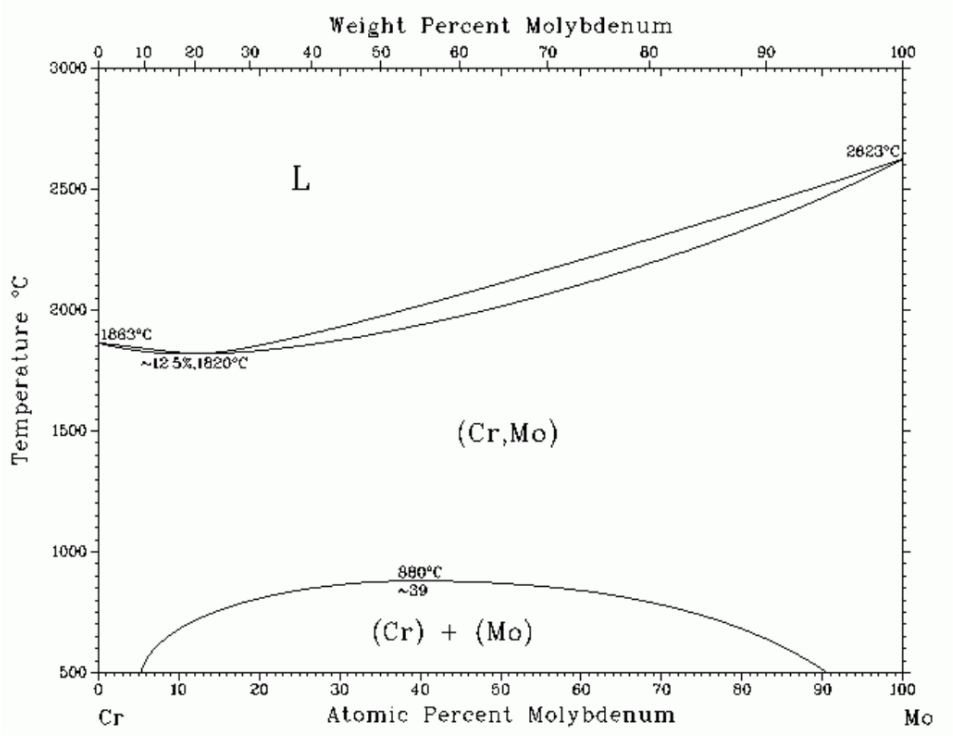

Figure 2.3 – Phase diagram Cr and Mo (VENKATRAMAN; NEUMANN, 1987).

widely used in the production of various alloys, where Chromium has been found to significantly improve the corrosion resistance and hardness of the resulting material, while Molybdenum enhances the strength and high-temperature performance. Therefore, despite the lack of studies specifically targeting the elemental system of Cr-Mo, their properties and behaviours in alloys can still provide useful insights for the development of dissimilar joints, surface modifications and other related applications.

2.5 Multiple reflections phenomena

The absorption behavior of laser radiation emitted by powdered materials differs from that of solid materials since, although metals have high reflectivity indices, they are more efficient when the energy received by the laser emission is absorbed.

This phenomenon, known as multiple reflections (KHAN; DICKENS, 2012) and is showed in Figure 2.4; consists of the fact that a fraction of the incident radiation encounters the upper surface of the dust particles, where part of it is reflected from the dust layer while the remaining portion gets absorbed. Simultaneously, another amount of incident radiation reaches the inner region of the dust, where it undergoes partial absorption and partial reflection back into the dust layer. Consequently, due to these successive reflections, the laser radiation can penetrate deep

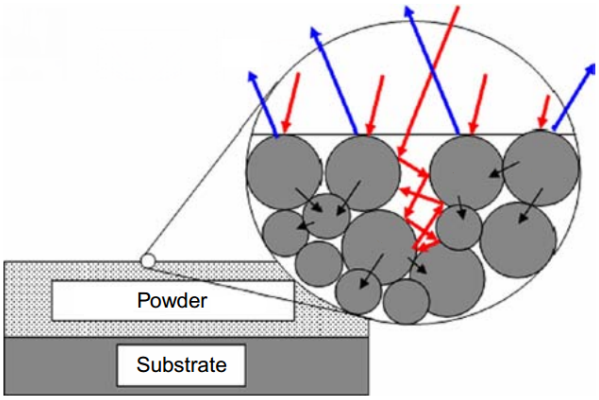

Figure 2.4 – Radiation absorption in powder bed (KHAN; DICKENS, 2012).

into the dust layer, surpassing the average diameter of the dust particles. This phenomenon entails multiple reflections as the radiation interacts with particles within the inner region of the pre-deposited powder layer, persisting until complete absorption is achieved (GUSAROV, 2020).

2.6 Fusion zone shape

The phenomenon of multiple reflections presented in section (REF) makes the energy emitted by the laser reaches the substrate and allows the fusion of the latter. During the fusion of both elements, powder, and substrate, a fusion well is produced where both components are mixed; depending on the amount of energy provided to the system, the formation of the fusion zone is different. In the case of this research, three appearances of the fusion zone were observed, U-formation, conduction, and keyhole. The following briefly describes each of the formations observed throughout the work.

2.6.1 Fusion zone U-shape

One of the variations of the fusion zone shape is the formation of a "U" in the laser-treated material; this formation is due to a phenomenon called splashing (ZAGADE *et al.*, 2021), where the centrifugal flows of Marangoni (KHAIRALLAH *et al.*, 2016) make the material to be expelled to the sides of the fusion zone thus leaving a "U" formation; This shape of the fusion zone occurs at low laser powers, also causing that when the material is fused in the powder layer, it remains agglomerated and does not allow the correct distribution in the fusion zone (XU *et al.*, 2014).

2.6.2 Conduction shape

The shape of the so-called conductive fusion zone is desired for the realization of dissimilar joints by additive manufacturing as well as for other processes such as laser surface modification; Because it generates a uniform fusion zone and an approximately continuous surface, it has advantages such as high process stability, decrease in defects such as pores and fractures due to minimized immediate vaporization of the materials and finally a good depth of penetration into either the previous layer or the substrate; an example of this shape in the fusion zone can be seen in the Figure 2.5 where Panwisawas *et al.* (2017) studied the differents fusion zone shapes.

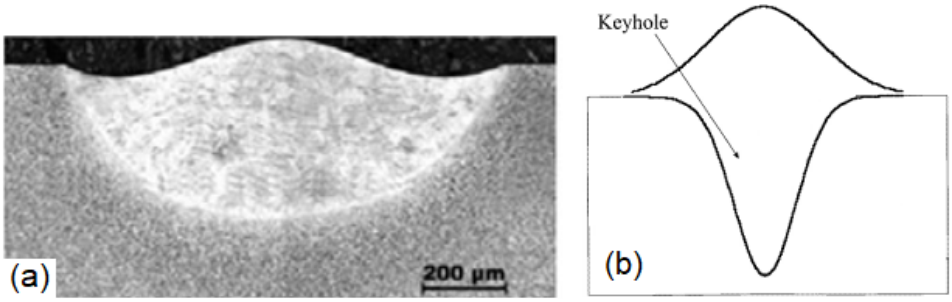

Figure 2.5 – Fusion zone shapes examples, conductive (a) and keyhole (b) (PANWISAWAS *et al.*, 2017).

2.6.3 Keyhole

The keyhole shape shown in Figure 2.5 is employed in laser additive manufacturing or processes where a high ratio of depth to width of the weld bead is desired. In this case, the high energy density provided by the laser is sufficient to vaporize the processed material and form plasma intensely. This process creates a cavity in the melt pool in the shape of a keyhole. The plasma formed above the surface of the processed material is called plume plasma, while the plasma formed in the keyhole cavity is called keyhole plasma (KIM *et al.*, 1995).

The keyhole shape's main challenge is the process's relative instability and the possible formation of porosity, which is generated by the collapse of the vapour cavity formed by metal vaporization. The stability of the keyhole depends on the balance between surface tension pressure and vapour pressure: surface tension pressure tends to close the keyhole. In contrast, vapour pressure tends to keep it open. Also, The keyhole mode is characterized by high penetration depth and high laser radiation absorption efficiency (PANWISAWAS *et al.*, 2017).

3 EXPERIMENTAL DETAILS

Detailed information is provided below on the techniques and procedures to identify the processed parts' characteristics and behaviour for this research. Figure 3.1 shows a general summary of the experimental process used to carry out this research.

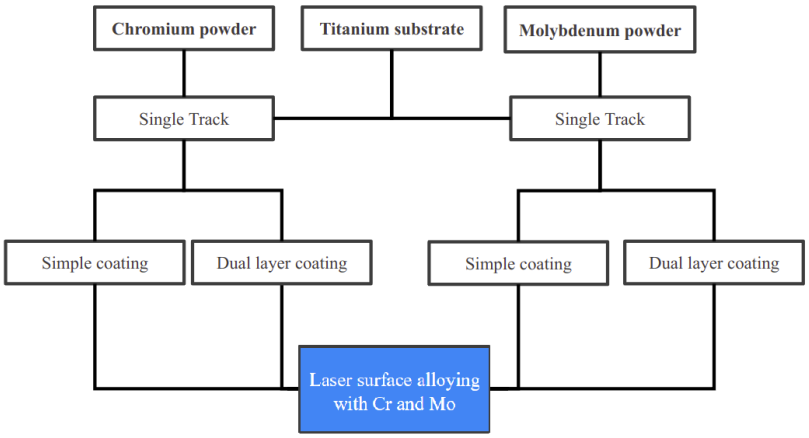

Figure 3.1 – Overview of experimental procedure.

3.1 Analysis of raw materials

In addition to the analysis of the Cr and Mo powders and the Ti substrate detailed in the following sections, a particle size analysis was carried out to determine the grain size of the powders mentioned above. To determine the particle size, a Laser Diffraction Analysis was performed in the Mastersizer-3000 equipment of the manufacturer *Malvern Instruments*, model MAZ3000 at the Laboratory of Biomass Characterization, Analytical, and Calibration Resources - LRAC. This analysis consists of making a suspension of the powder of interest utilizing compressed air and measuring the volume density by the laser's diffraction when it enters the sample.

3.2 Laser and own-design equipment

To carry out all the necessary tests for the study of the compatibility between the elements, substrate Ti with Mo and Ti with Cr, equipment of the company *MBraun* was used, which

consists of several elements as shown in figure 3.2 (a), among them a glovebox chamber that allows the control of the atmospheric composition. Due to the interference of the oxygen in the environment with the final result of the titanium laser treatment (LI *et al.*, 2005), the atmosphere is controlled with a positive pressure of Argon, purified by the absorption of oxygen by a filter bed that allows having an inert and controlled atmosphere.

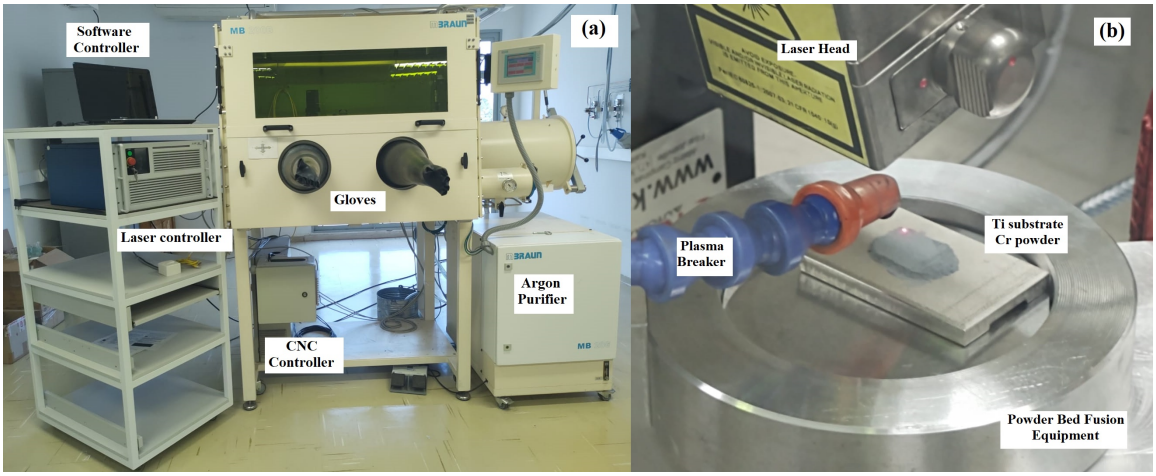

Figure 3.2 – Laser and environment controller, glovebox MBraun (a) and own-designed powder bed fusion equipment (b).

For the use of the elements to be used in the tests, there are two gloves that allow the manipulation inside the chamber. Inside the glovebox, there is a CNC table that allows the movement of the piece to be treated with the laser in the X-axis and Y-axis, this movement is controlled by the *Match3* software that facilitates the movement that was used for the manufacture of individual single laser tracks, and single and double layers. There is also a fixed laser head, where the focal distance can be manipulated.

Table 3.1 – Used materials reflection coefficient (STEEN; MAZUMDER, 2010).

Material	**Coefficient of reflection (at 1,06 μm)**
Chromium	0,519
Molybdenum	0,689
Titanium	0,629

The laser used is a Ytterbium Fiber laser (IPG Photonics, model YLR) with a maximum power of 500 W and emitting at a wavelength of 1.06 μm. Table 3.1 shows the reflection coefficient parameters for each element to be used.

Inside the equipment described above, there is a own-designed instrument, which, with a micrometer, allows to modulate of the height of a cylinder, allowing to regulate, at the discretion

of the researcher, of the thickness of each layer of powder to be treated with laser on a particular substrate, in this case, a titanium plate, the equipment can be see in Figure 3.3 and the result of process can be seen in Figure 3.2 (b).

Figure 3.3 – Own design equipment installed inside of glovebox.

3.3 Single laser tracks and coating fabrication of both systems

Initially, pieces of the original plates were cut 50 mm long, where they had machined recesses, 1.5 cm wide and 0.25 mm deep, that depth was selected from , on the surface of the Ti plate; the depth was selected from previous works((CARVALHO *et al.*, 2018; LEVA, 2016; FOGAGNOLO *et al.*, 2013; FOGAGNOLO *et al.*, 2016). Subsequently, the sheets were sanded with Si-C paper (1200 mesh particle size) and subjected to ultrasonic cleaning in a 95% ethyl alcohol solution (LEVA, 2016). Next, the recesses in the sheet were filled entirely and carefully with Cr and Mo powder in separate pieces to avoid contamination. Figure 3.4 illustrates the procedure used to fabricate the single laser track. Finally, the samples were prepared for metallography following the ASTM normtivity (TESTING; (FILADELFIA, 2009).

To perform metallography, we cut the plate perpendicular to the direction of laser beam displacement using a diamond disk. Afterwards, we embedded the plate in hot curing resin and manually ground it using SiC-based sandpaper with a mesh from 100 mesh to 1200 mesh. We then polished the samples in two steps. First, we used a 3 μm cloth and 9, 6, and 3 μm diamond paste. Then, we polished the pieces with a 0.5 μm silica suspension solution in the VibroMesh.

3.3.1 Coating manufacturing strategy

To manufacture the individual coating for each of the Ti-Cr and Ti-Mo systems, a implementation using *GCode* was developed, which is used by the *Match3* software mentioned

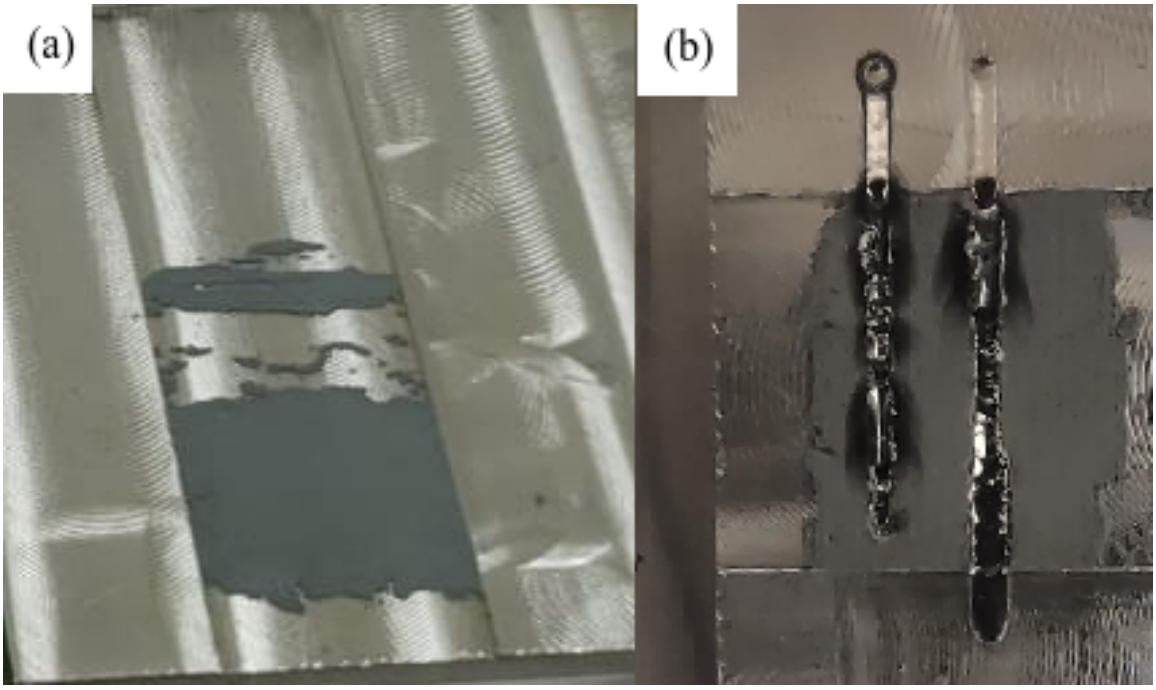

Figure 3.4 – Ti substrate filled with Mo before laser treatment (a) and single laser track 300 W and 450 W (b) after modification.

in section 3.2 to coordinate the movement of the CNC. Figure 3.5 (a) graphically shows the sequence in which the laser was used to make the coating with a single layer. Subsequently, for the surface modification with two layers, the sequence shown in Figure 3.5 (b) is used, and this change in the sequence corresponds to the strategy to simulate the conditions in which the sample could be made in an automatic additive manufacturing equipment.

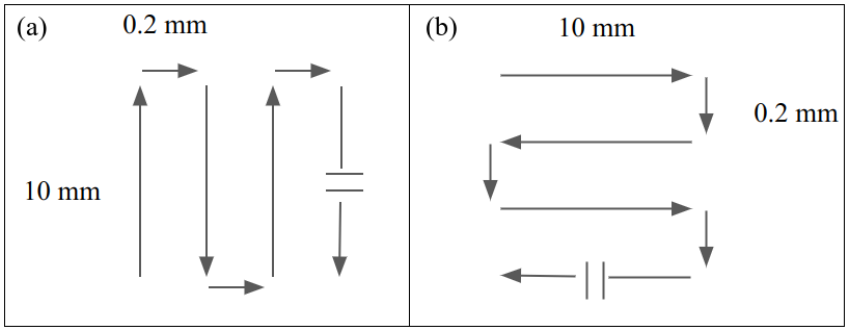

Figure 3.5 – Graphical secuence to one layer (a) and second layer (b) used by CNC from *Match3*.

3.4 Characterization techniques

For the characterization of the samples, we used the following techniques.

3.4.1 Optical and scanning electron microscopy (SEM)

The microstructural characterization of the Ti plates and the metallography were performed using optical microscopy. For this, a reflected light optical microscope from Carl Zeiss, Axio Scope model was used. The microstructure present in the fusion zone of the Ti-Cr and Ti-Mo alloys single laser tracks and coatings were analyzed by scanning electron microscopy in the backscattered (BSE electron mode. For this, a Carl Zeiss EVO-MA15 microscope was used, with BSE and secondary electron detectors, presented in the Figure 3.6.

Figure 3.6 – Scanning electron microscope (SEM) Carl Zeiss EVO-MA15.

The qualitative morphological characterization of the Cr and Mo powders was also performed by scanning electron microscopy, but in the secondary electron mode. For this purpose, small amounts of the powders were adhered to a conductive carbon tape. The advantage of using backscattered electrons is that the intensity of the signal depends on the atomic number of the material (chemical contrast (MARENZI *et al.*, 2019). Because of this, it was possible to obtain information about the distribution of the alloying element in the fusion zone.

3.4.2 Energy Dispersive X-ray Spectrometry (EDS)

In addition to the analysis by BSE mode, the SEM has an X-max detector from Oxford Instruments, which allows Energy Dispersive X-Ray Spectrometry (EDS) analysis, which helps to obtain qualitative and quantitative results of the sample in question (JOY *et al.*, 1986), thus

allowing to have the idea of the distribution of the elements in the fusion zone, in addition, to quantify these elements even in minimal points and to identify with certainty and indirectly the phases that may be present in the sample.

3.4.3 X-Ray Diffraction (XRD)

X-ray diffractograms were performed on the Ti substrate (LEVA, 2016) and analogously on the Cr and Mo powders to have certainty of the crystalline phases present in the raw materials. Additionally, we performed X-ray diffractograms on the surface to identify the crystalline phases present in the sample initially manufactured with a Mo layer and subsequently modified on the surface by depositing an additional layer of Cr. Then, we removed approximately a 50 μm layer of the sample and conducted a new XRD analysis. For this purpose, we used a Panalytical X'pert PRO diffractometer with a Cu anode and a PIXcel ultra-fast detector. We led the measurements with a voltage of 40 kV and a current of 30 mA. To prepare for analysis, we lightly polished the surface to eliminate the majority of surface roughness.

3.4.4 Mechanical tests

Finally, to get an idea of some of the mechanical properties obtained by the addition of Mo and Cr on the surface of the Ti substrate, microhardness and instrumented indentation analyses were performed to obtain hardness and Young's modulus values on both the sample and the individual Ti-Cr and Ti-Mo coatings to compare the variation between the layers.

3.4.4.1 Microhardness

The Vickers Hardness of the Ti substrate and that of the Ti-Cr and Ti-Mo systems was determined using the indentation method. Additionally, the Vickers Hardness of the Ti surface with two modifications was evaluated: an initial Mo layer followed by a second layer of Cr over Mo. The *Future Tech* Vickers Hardness tester, model FV-800, was employed for this purpose. The diamond penetrator has a square-based pyramidal geometry with a 136° angle between the opposite faces. Before indentation, the samples were carefully polished following the guidelines outlined in ASTM E384-16 (TESTING; MATERIALS, 2017). Each indentation was repeated 15 times, applying a load of 4.9 N (0.5 *Kgf*) and maintaining the pressure for 15 seconds per indentation. Finally, the average hardness and standard deviation were calculated based on the

results obtained from the 15 indentations. The Vicker Hardness tester can be seen in Figure 3.7 (b).

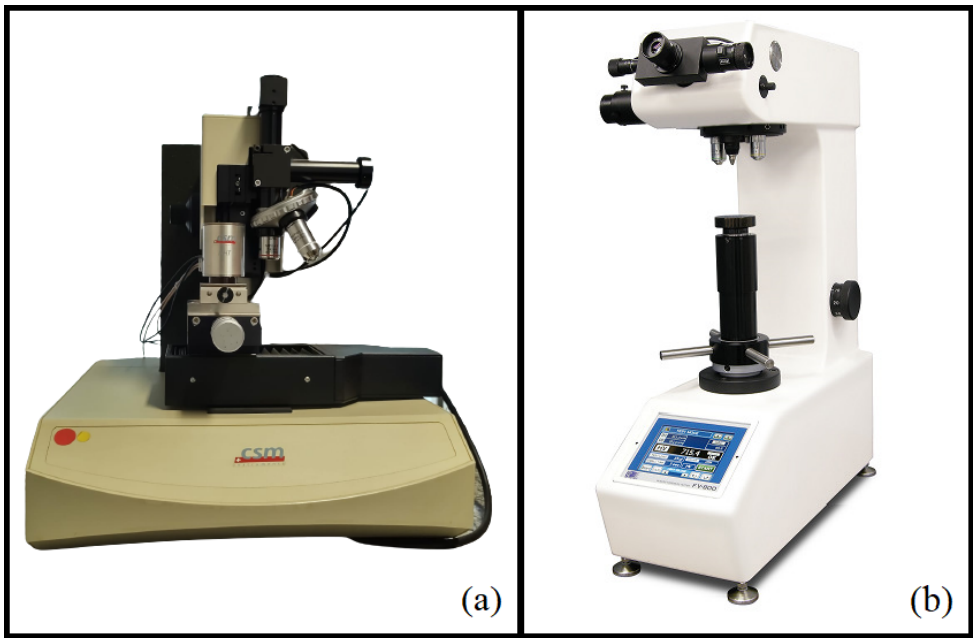

Figure 3.7 – CSM indentation instrument NHT1 (a) and Vickers harndess tester FV-800 (b).

3.4.4.2 Instrumented indentation

CSM model NHT1 instrumented indentation equipment was used to determine hardness and modulus of elasticity from the surface to the inside of the part, with a Berkovick-type diamond indenter operated with a load of 400 mN for the 30s.The hardness and modulus of elasticity were determined using Oliver and Pharr's method, considering Poisson's coefficient value of 0.3. This analysis was conducted to assess the mechanical behaviour of the resulting modification. Five measurements were made varying the depth from the surface; for this purpose, a transversal cut was made to the piece, and it was embedded in resin to be later submitted to metallography following the parameters and indications of the ASTM E3-01 (TESTING; (FILADELFIA, 2009) standard. Five indentations were made varying the depth measured from the surface, starting at 25 μm and advancing 50 μm towards the substrate; at these depths, five indentations were made horizontally with an approximate separation of 50 μm to have an average value and a standard deviation. In Figure 3.7, you can see the equipment used since the surface to be analyzed is relatively tiny to use micro indentation.

4 RESULTS AND DISCUSSION

The titanium plates (Cp) used in this work were obtained from the research carried out by Leva (2016) in the laser materials processing laboratory, so the results of the analysis of the raw material of the titanium plates have been included and referenced.

4.1 Raw Materials

In addition to the titanium plates (Cp), fine chromium and molybdenum powders were used, coming from the companies *Alfa Aesar* and *ThermoFisher Scientific*. A rectangular shape Ti-CP sheet with a 10 cm side was used as a substrate provided by Titânio Brasil. X-ray fluorescence (XRF) was used by Leva (2016), to measure the purity of the titanium sheets; the results indicated that the titanium sheets had over 99% purity. The certificates of analysis of these powders can also provide the percentage of purity, and could be appreciated on the table 4.1.

Table 4.1 – Purity of raw materials, titanium data from Leva (2016)

Material	**Purity according to supplier (%)**	**Supplier**	**XRF Purity (%)**
Titanium plates	99.9	Titanium Brasil	99.5
Cr powder	99.0	Alfa Aesar	-
Mo powder	99.95	ThermoFisher	-

4.1.1 Titanium sheets

The figure 4.1 shows the microstructure of the Ti substrate used in the experiment. Grain equiaxed and macules were present on the substrate. As can be seen in the optical microscopy image, the substrate was mechanically deformed and then heat-treated to recrystallize and grow grains. Image taken by Leva (2016).

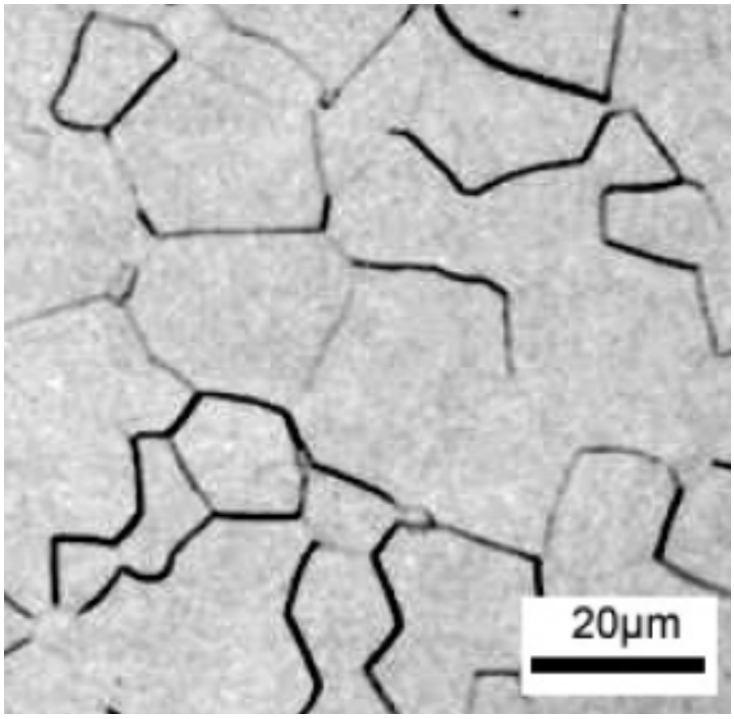

Figure 4.1 – Ti (Cp) substrate microstructure, via optical microscopy.

In addition to optical microscopy, Figure 4.2 shown the X-ray diffraction analysis is obtained, where a concordance of the peaks with the crystallographic record of titanium is observed (WYCKOFF, 1963), having as reference a compact hexagonal microstructure, characteristic of titanium.

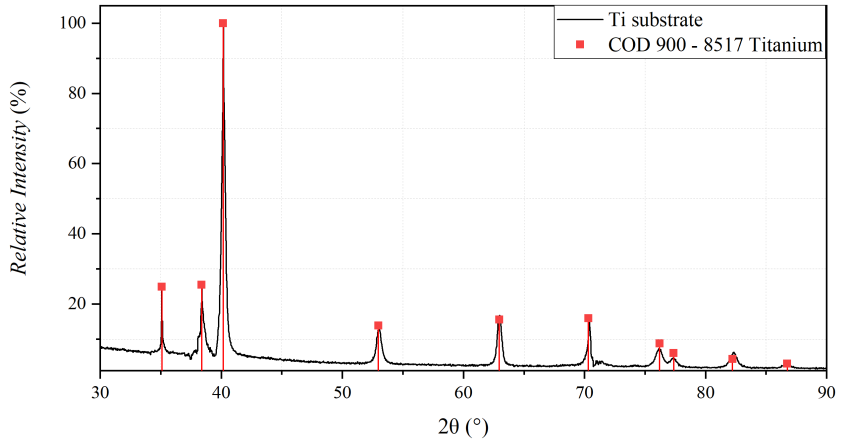

Figure 4.2 – X-Ray Diffraction from Ti substrate compared with COD 900 -8517 pattern.

4.1.2 Chromium and molybdenum powders

Figure 4.3 shows Scanning Electron Microscopy (SEM) in secondary electron scanning mode, images of the Cr (a) and Mo (b) powders, both showing an irregular morphology, also suggesting that Mo particles have agglomerated together.

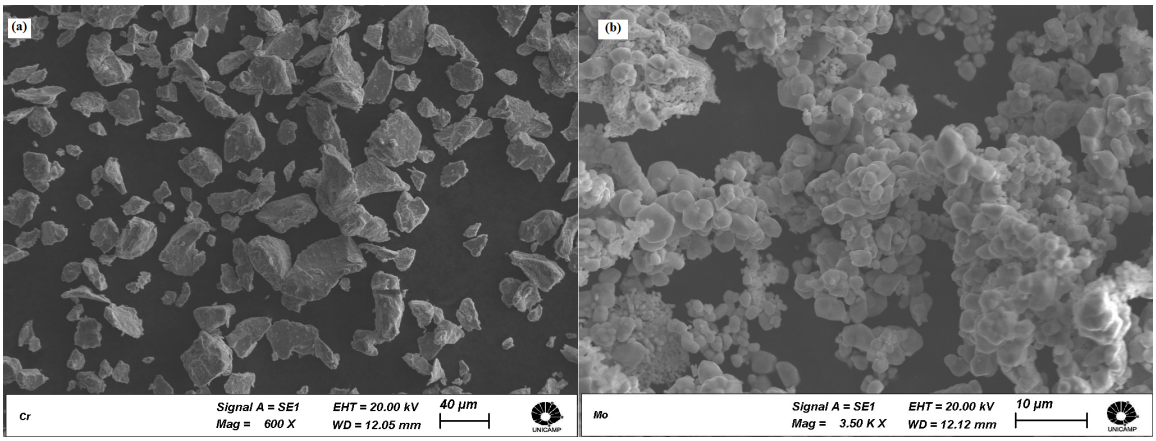

Figure 4.3 – SEM images Cr (a) and Mo (b) powders, Secondary Electron Scanning mode.

Figure 4.4 shows the particle size distribution of Cr and Mo powders obtained by the laser diffraction technique. From the comparative analysis of these results, it was concluded that the particles of Cr powder showed a narrower particle size distribution than that of Mo powder.

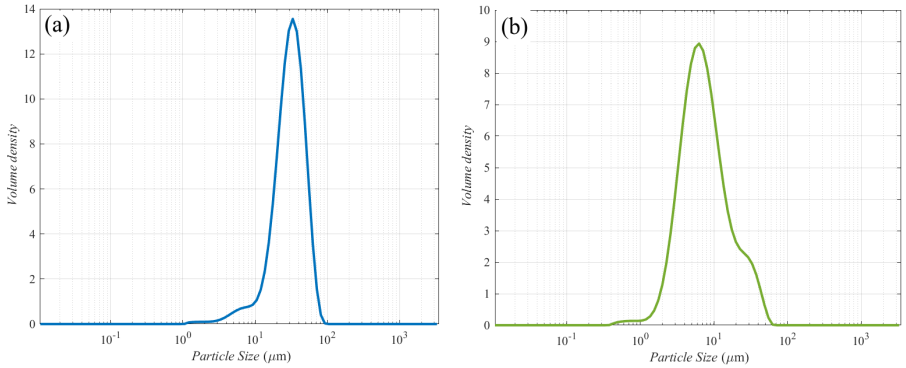

Figure 4.4 – Particle distribution size Cr (a) and Mo (b) powders.

However, the average particle size of Cr is larger than that of Mo. The $D_{0.1}$, $D_{0.5}$, and $D_{0.9}$ values of the Cr and Mo powders are shown in Table 4.2.

Table 4.2 – $D_{0.1}$, $D_{0.5}$, and $D_{0.9}$ Particle distribution size by laser diffraction test.

Material	**D**$_{0,1}$ **(**μ**m)**	**D**$_{0,5}$ **(**μ**m)**	**D**$_{0,9}$ **(**μ**m)**
Cr powder	15.03	30.63	51.43
Mo powder	3.05	6.93	21.83

Finally, just like the Ti substrate used in this work, the Cr and Mo powders were subjected to an XRD analysis to determine the similarity between the crystalline phases in each of the powders. Figure 4.5 shows the obtained diffractogram for the Cr sample (a) and Mo (b), contrasting the most relevant peaks. We can observe that both exhibit a correspondence with their crystallographic card JCPDS 42-1120 to Mo (SCHREINER, 1989; LEVA, 2016). Similarly, Cr can be compared to the crystallographic card COD 500-0220 (SWANSON *et al.*, 1953; BUSCAIL *et al.*, 2004).

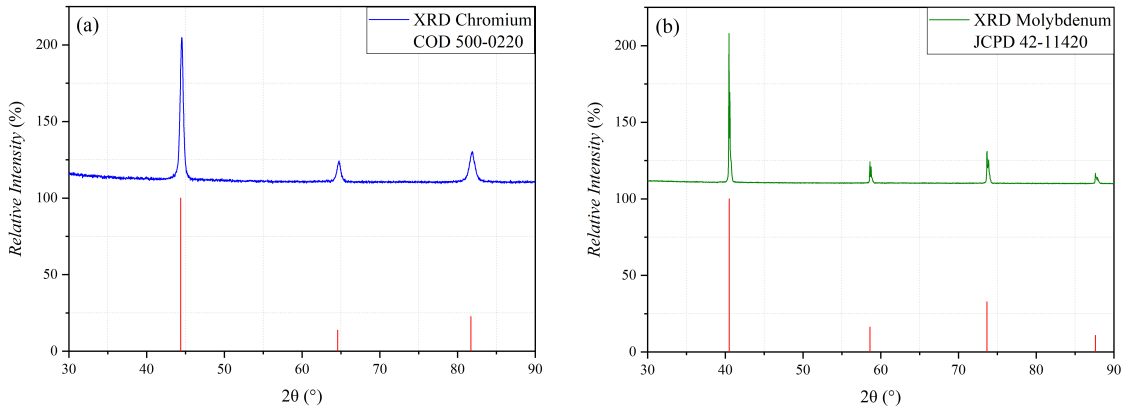

Figure 4.5 – XRD from Cr (a) and Mo (b) powders.

As a first step toward evaluating the compatibility between elements, tests were carried out on a pair of tracks, in this case, Cr single laser track was manufactured on the Ti substrate and likewise Mo on Ti; varying the laser power. An overview of the results of these tests, comparing them with each other, is presented, giving an understanding of the changes resulting from a change in element type. This work reaches Cr with Mo on a Ti sheet.

In addition, Figure 4.6 summarizes the single laser tracks carried out by varying the laser power between 150 W and 450 W, keeping the following parameters constants in all tests: CNC speed at 10 mm/s, laser diameter 0.2 mm and layer thickness at 0.25 mm, for the two systems, followed by the analysis of Ti-Cr and Ti-Mo for each laser power used.

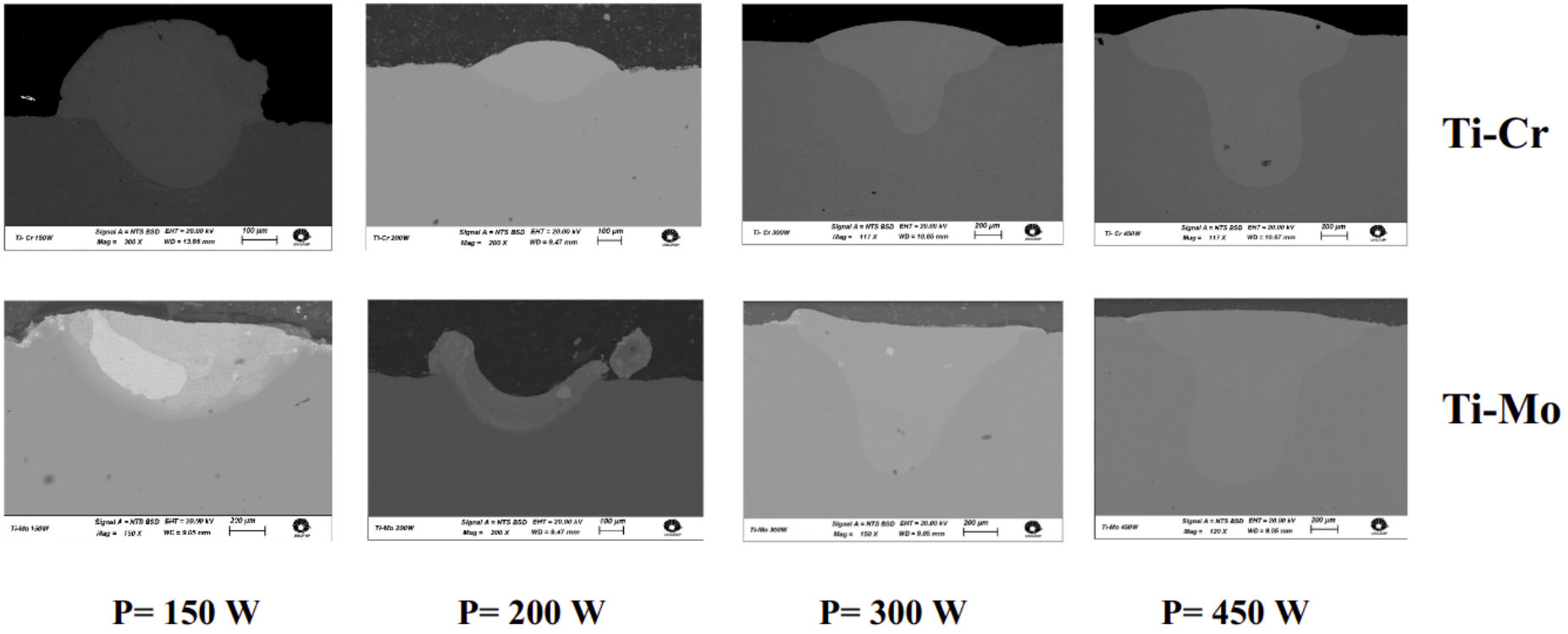

Figure 4.6 – Overview of single laser tracks made for each system and varying laser power.

4.2 Ti-Cr, and Ti-Mo 150 W single laser track.

Figure 4.7 shows a comparison between Cr and Mo single laser tracks, showing a difference in the shape resulting from the laser treatment at 150 W power; for Cr, a conduction form is noticed as a result of the low power input (150 W), which makes the fusion zone small, and little amount of Ti is affected by it. n the case of Mo, the low power results in lack of fusion due its hight fusion temperature, that is approximately 1000°C higher than that of Ti (MURRAY, 1981b), which finally makes Mo dont fuse completelly.

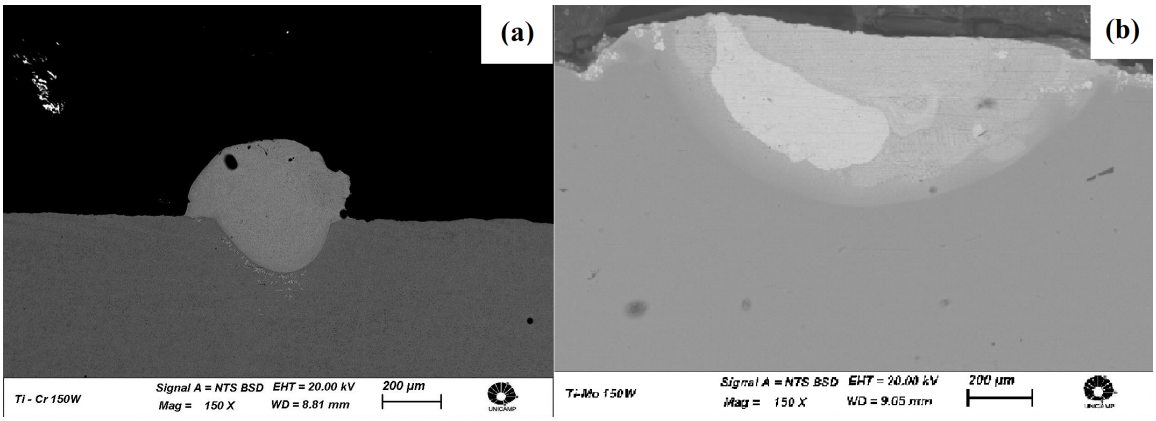

Figure 4.7 – Ti-Cr (a) single laser track, compared with Ti-Mo (b) at 150 W laser power.

As shown in Figure 4.7 (a), the two elements have no differentiable phases, and it appears to be a homogeneous solution. However, a closer examination reveals variations in the microstructure along the single laser track. Figure 4.8 (a) illustrates this. A fusion zone exhibits microsegregation, along with a uniform area.

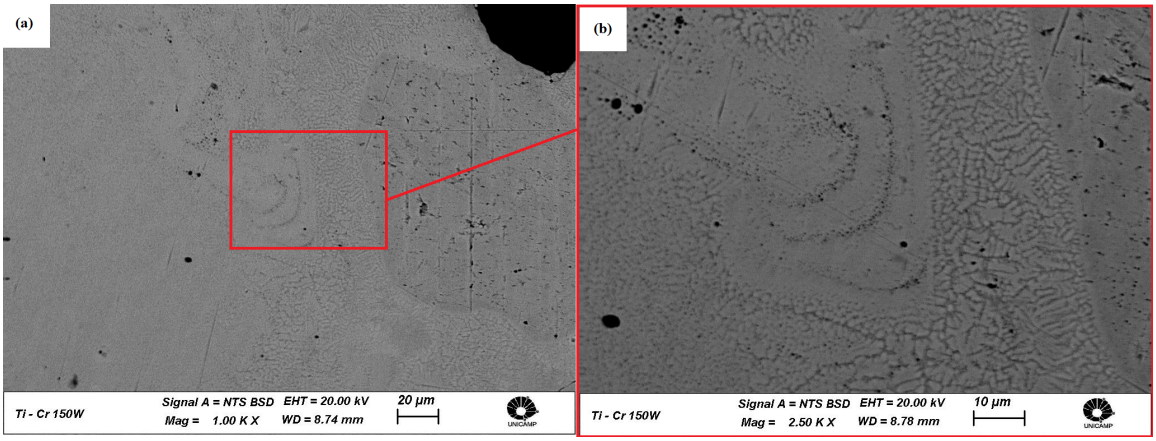

Figure 4.8 – SEM microsstructures observed in Ti-Cr single laser track using 150 W of laser power.

In the case of Mo (Figure 4.7 (b)), as reported in the literature ((LEVA, 2016; MOHAN *et al.*, 2021; KURODA *et al.*, 2016)), the formation of the β-Ti phase can be observed, with Mo being a stabilizer of this stable phase.

Table 4.3 – Width and depth of the Ti-Cr and Ti-Mo fusion zones using 150 W of laser power.

Sample 150 W	**Width (μm)**	**Depth (μm)**
Ti - Cr	425	109
Ti - Mo	354	89

Comparing both fusion zones, Table 4.3 shows that the fusion zone is slightly more profound for Cr than the one generated in the Ti-Mo single laser track. This is because the melting temperature of Cr is close to that of Ti, causing more of the substrate to be melted and generating a greater depth in the melting zone. However, in addition to the depth, we also see that the width in both samples is similar, only differing in the formation after laser treatment.

Mapping by Energy Dispersive X-Ray Spectroscopy (EDS), as seen in Figure 4.9, we know the distribution of the elements along the single laser track for Cr, where Ti is observed in yellow (b) and Cr in cyan (c). Furthermore, from the image, it can be noticed that has a Cr accumulation at the sides of the fusion zone, where the microstructure observed in Figure 4.8 (b) is of uniform appearance, an absence of Ti, according to Khairallah *et al.* (2016), this due to the Marangoni flows convection.

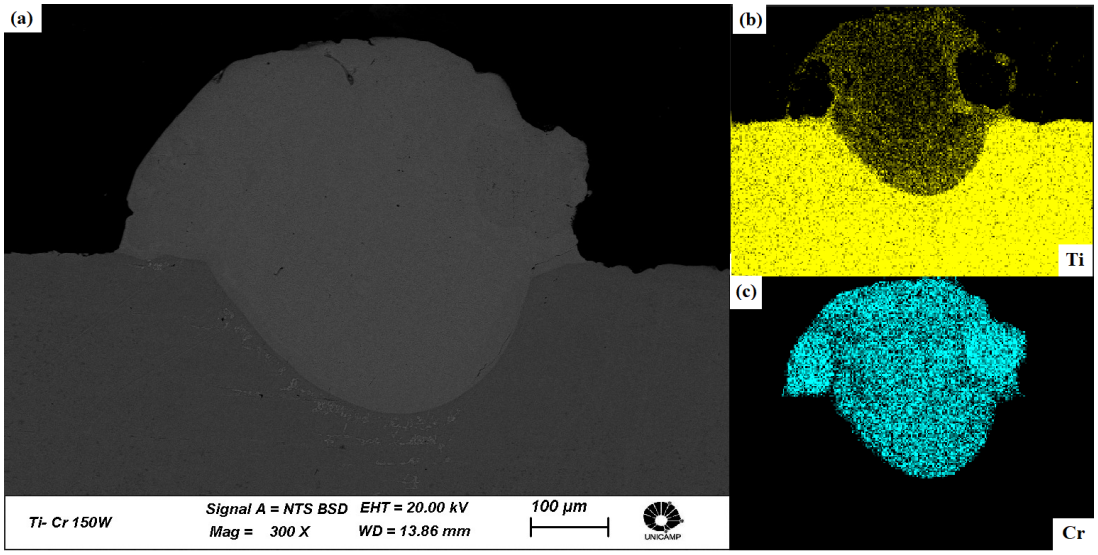

Figure 4.9 – EDS map analysis of TI-Cr single laser track 150 W of laser power. Ti (b) yellow, and Cr (c) cyan.

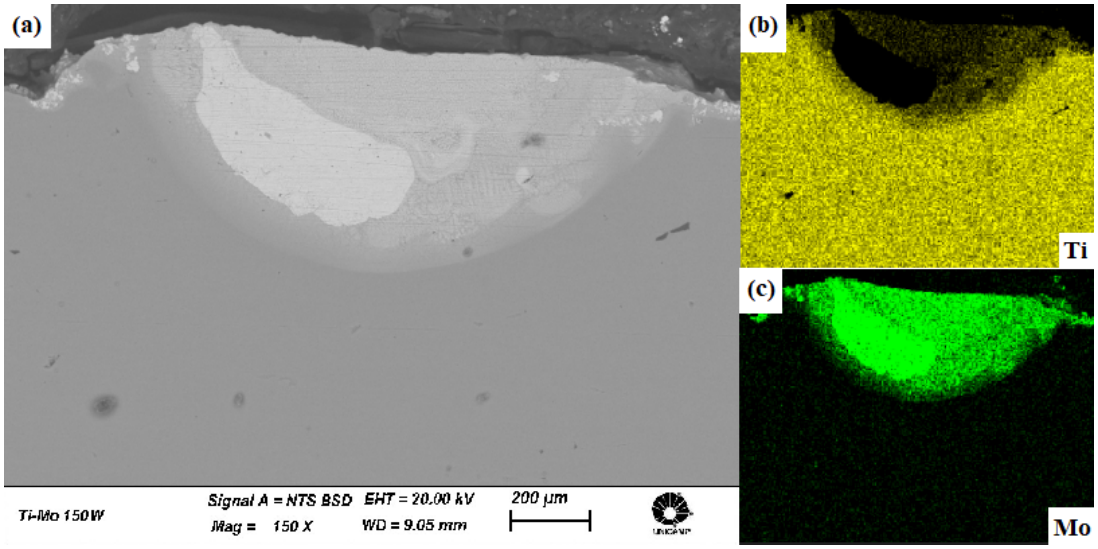

Figure 4.10 – EDS map analysis of TI-Mo single laser track 150 W laser power.Ti (b) yellow, and Mo (c) green.

On the other hand, in Figure 4.10, we see the distribution of the elements in single laser track for Ti-Mo, as with Cr, Ti appears yellow (b), and on the other hand, Mo is green (c). The area in the absence of Ti is an unmelted particles of Mo due to the low power applied in this test. However, Boley *et al.* (2015) mentions the effect of absorption by multiple reflections; in this case, it is insufficient to generate a uniform distribution of Mo in Ti.

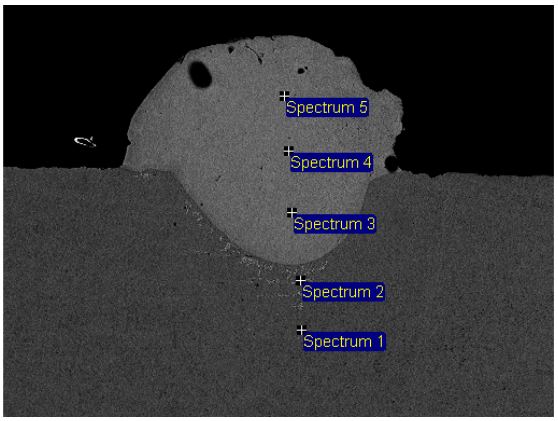

Spectrum	Ti	Cr
Spectrum 1	100	0
Spectrum 2	100	0
Spectrum 3	19.5	80.5
Spectrum 4	17.9	82.1
Spectrum 5	10.1	89.9

Figure 4.11 – EDS point analysis of TI-Cr single laser track 150 W laser power. Values in weight percent.

In addition to the EDS mapping, several point analyses of the concentration of each element in the corresponding single laser track were performed, yielding the results presented in Figure 4.11 for Cr and Figure 4.12 for Mo.

A change in Ti composition is not observed throughout the sample, this is because a homogeneous mixture is generated between the elements during the application of the laser

power. All values are in percent/weight.

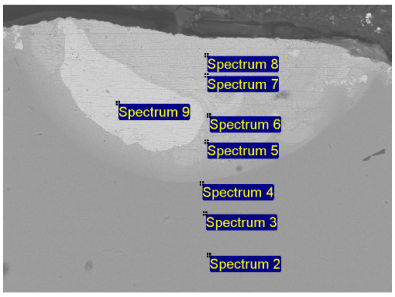

Spectrum	Ti	Mo
Spectrum 2	100	0
Spectrum 3	100	0
Spectrum 4	100	0
Spectrum 5	57.4	42.6

Spectrum	Ti	Mo
Spectrum 6	41.4	53.6
Spectrum 7	32.5	67.5
Spectrum 8	32.7	67.3
Spectrum 9	0	100

Figure 4.12 – EDS point analysis of Ti-Mo single laser track 150 W laser power. Values in weight percent.

In the same way as in Figure 4.11 for Cr, in the case of Mo (Figure 4.12), the exact change in concentration is observed. However, the difference in concentration is a higher than compared with Ti-Cr. Taking into account the melting point of Cr (1863°C) and Mo (2623°C) (STEEN; MAZUMDER, 2010); Mo needs a higher amount of energy (in this case from the laser) to reach its melting point, which means that a smaller amount of Mo is mixed with the molten substrate and generates a lower concentration of Mo in the fusion zone and, in addition, unmolten particles of Mo.

4.2.1 Ti-Cr 150 W crack in the interface.

Finally, Figure 4.13 shows the image of the fracture at the interface between Ti substrate and fusion zone, having dendritic-like microstructures extending close to the fracture surface. Complete separation and analysis of the fracture surface could help to verify the phases that comprise the fracture since, according to Thomas *et al.* (2020), several phases can be present in the mixture between Ti and Cr, all with different properties, especially the intermetallic compound $TiCr_2$ which has a higher Vickers hardness than its other faces.

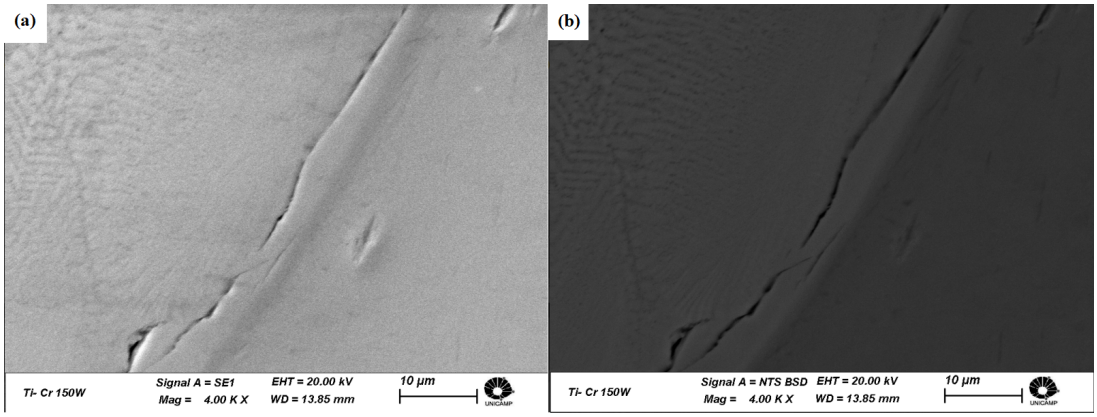

Figure 4.13 – SEM crack image in the interface between Ti-Cr fusion zone and Ti substrate. Secondary electron mode (a) and BSE mode (b).

4.3 Ti-Cr, and Ti-Mo 200 W single laser track.

As for the test in section 4.2, two single laser tracks were manufactured using 200 W power, one with Ti-Cr and the other with Ti-Mo, both analyzed by SEM in BSE mode to have a better visualization of the distribution of the fusion zones on the Ti substrate, then in the Figure 4.14 is shown a comparison between the single laser track, made with a of 200 W laser power.

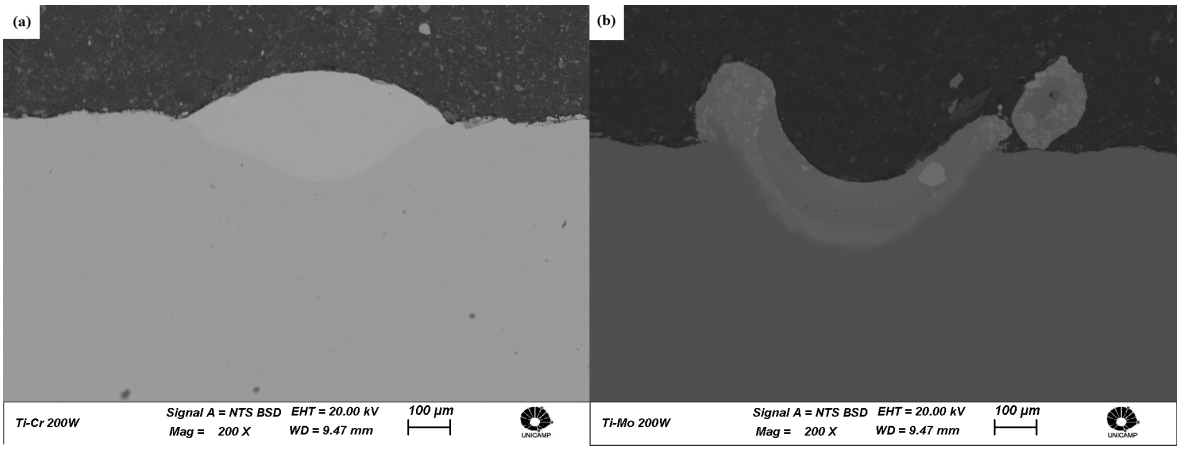

Figure 4.14 – Ti-Cr (a) single laser track, compared with Ti-Mo (b) at 200 W laser power.

In Figure 4.14, Cr, and Mo single laser tracks are compared to show the differences in fusion zone caused by laser treatment at 200 W. For Cr, a form of conductivity results from increasing the laser power, observing the apparent compatibility between the two elements. On the other hand, for the Mo single laser track, a U-shape is obtained in the fusion zone, contrasting with the literature (KIM *et al.*, 1995; LEVA, 2016). As power increased, the maximum temperature reached in the fusion zone increased, and the back pressure increased as alloying

elements and substrates vaporized (SEMAK; MATSUNAWA, 1997). Back pressure pushes the fusion zone liquid downward, causing the fluid to escape through the sides, a process known as liquid expulsion, leaving a U-shaped fusion zone (DRAPER; EWING, 1984).

Table 4.4 – Width and depth of the Ti-Cr and Ti-Mo fusion zones using 200 W of laser power.

Sample 200 W	**Width (μm)**	**Depth (μm)**
Ti - Cr	616	144
Ti - Mo	595	241

In the Ti-Cr system, Figure 4.14 (a) does not show an apparent differentiation of the phases; even with a closer approach, no evident changes in microstructure are observed. On the other hand, in Figure 4.14 (b), it can be seen that, as in Figure 4.7 (b), despite the increase in laser power, it shows Mo unfused particles in the fusion zone; the rise in laser power was insufficient for the complete fusion of Mo and mixing of Ti with Mo. However, it was enough to change the format of the fusion zone.

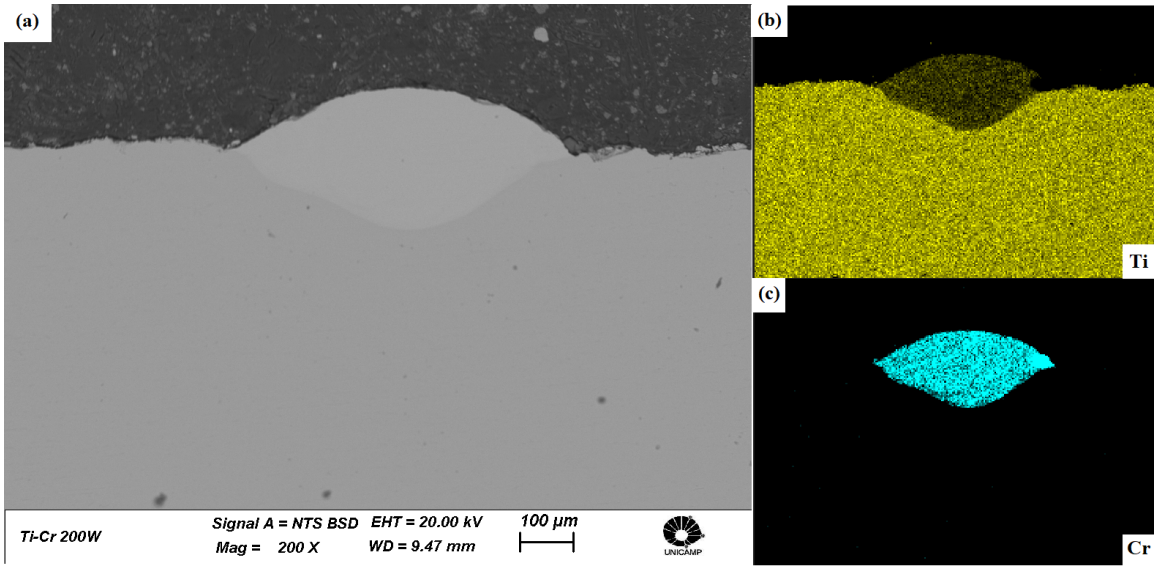

Figure 4.15 – EDS map analysis of TI-Cr single laser track 200 W laser power. Ti (b) yellow, and Cr (c) cyan.

Measuring the width and depth of the fusion zone can be observed in Table 4.4, an increase in both parameters for each element; also having a particular case in which the fusion zone of the Ti-Mo single laser track, where the increase in depth was approximately three times compared to the depth presented in Table 4.3. The above agrees with the postulated by (BOLEY *et al.*, 2015), making Mo more efficient at the time of absorption of the energy produced by the laser,

increasing the efficiency of heat transfer to the substrate, and resulting in the U-shape and increase in the depth of the fusion zone, as mentioned above.

Based on EDS mapping, as shown in Figure 4.15, where Ti is showed in yellow (b), and Cr is visible in cyan (c), the fusion zone has a concentration of Cr at the right side due to the phenomenon of liquid expulsion (SEMAK; MATSUNAWA, 1997).

In the same manner as for Cr, mapping by EDS, as seen in Figure 4.16, we know the distribution of the elements along the single laser track for Cr, where Ti is observed in yellow (b) and Mo in green (c).

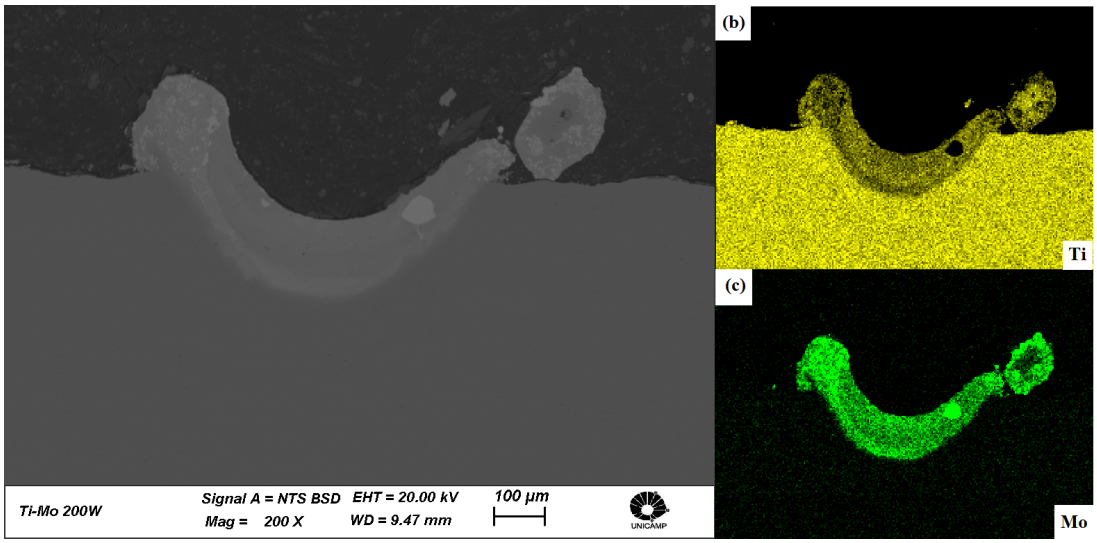

Figure 4.16 – EDS map analysis of TI-Mo single laser track 200 W laser power. Ti (b) yellow, and Mo (c) green.

The increase in power generated a better distribution of Mo along the fusion zone; a difference can be observed between the U-shaped surface and the interface on the left side of the fusion zone. However, it also presents an unmelted particles of Mo on the right side, demonstrating that the energy provided by the laser was not enough to generate a complete mix between Ti and Mo. In addition, as mentioned above (SEMAK; MATSUNAWA, 1997), back pressure pushes the fusion zone liquid downward, causing the fluid to escape through the sides, a process known as liquid expulsion, leaving both sides of the fusion zone more concentrated in Mo.

In the same way, as in the 150 W laser power single laser track, a EDS point analysis was performed along the fusion zone to have an idea of the distribution of the elements along it; they are presented in Figure 4.17 for Cr and finally for Mo in Figure 4.18.

From Figure 4.17, we can observe that there is an apparent homogeneous distribution

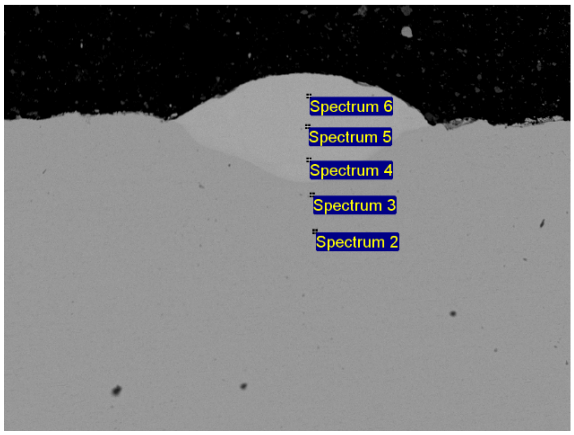

Spectrum	Ti	Cr
Spectrum 2	100	0
Spectrum 3	100	0
Spectrum 4	41.5	58.6
Spectrum 5	41.1	58.9
Spectrum 6	41.1	58.9

Figure 4.17 – EDS point analysis of Ti-Cr single laser track 200 W laser power. Values in weight percent.

along the melting zone, regardless of the accumulation of chromium at one end; we can also note that there are no significant changes in the concentration of the elements as one approach from the bottom of the melting zone towards the surface, as observed in Figure 4.11. The increase in power allows a better distribution of Cr on the Ti sheet.

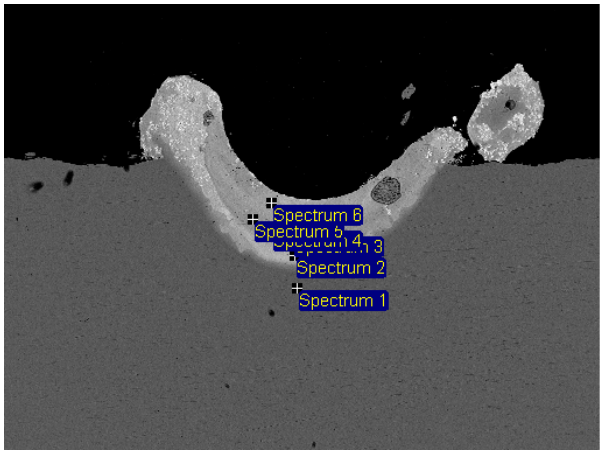

Spectrum	Ti	Mo
Spectrum 1	100	0
Spectrum 2	53.6	46.4
Spectrum 3	72.0	28.0
Spectrum 4	69.8	30.2
Spectrum 5	70.4	29.6
Spectrum 6	62.1	37.9

Figure 4.18 – EDS point analysis of Ti-Mo single laser track 200 W laser power. Values in weight percent.

On the other hand, in Figure 4.18, we can observe a distribution that varies along the fusion zone, having Mo unmelted particles by lack laser power in some sectors; those zones where a bright colouration is observed indicate high concentration of Mo, those zones present an absence of Ti in its composition and microstructure.

Comparing the concentrations along the fusion zone, Figure 4.18 and spectrum 5 of Figure 4.12, we can observe that, as well as the 150 W single laser track, Cr has a higher distribution along the fusion zone than the concentration of Mo found in the sample, due to the reflectivity

of Mo, more Ti substrate is melted, and there is a more significant dilution of Mo in the fusion zone. On the other hand, the fusion temperatures of Ti and Cr being very close (MURRAY, 1981a) allows the formation of a homogeneous solution and may have a better mixing between them.

4.4 Ti-Cr, and Ti-Mo 300 W single laser track.

As for the previous laser powers (150 W and 200 W), SEM analysis was performed in BSE mode to observe the shape and distribution of the elements in the test body; Mo reflects electrons more intensely than Ti due to its higher atomic mass. Figure 4.19 compares Cr and Mo single laser tracks, showing a similarity in shape resulting from the laser treatment at 300 W laser power.

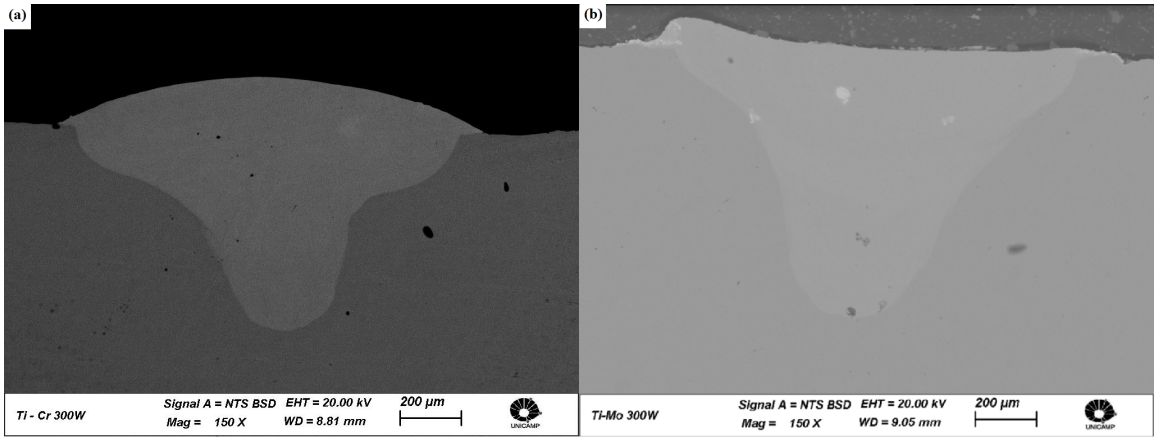

Figure 4.19 – Ti-Cr (a) single laser track, compared with Ti-Mo (b) at 300 W laser power.

According to information provided by Kim *et al.* (1995), the form presented for both laser treatments is a transition between conduction and keyhole shape, making the fusion zone deeper for every single laser track. In the case of Mo (Figure 4.19 (b)), pores are generated at the bottom of the fusion zone, caused by the evaporation of small amounts of substrate. In addition, small Mo unmelted particles are observed at the top of the fusion zone.

Table 4.5 – Width and depth of the Ti-Cr and Ti-Mo fusion zones using 300 W of laser power.

Sample 300 W	**Width (μm)**	**Depth (μm)**
Ti - Cr	1323	684
Ti - Mo	1308	867

Making a comparison in the measurement of the parameters of width and depth of the fusion zone of both single laser tracks, we can find in Table 4.5 that in both cases, the width is similar, having a slight difference between them, 200 μm; however, when comparing the depth, we find that there is a considerable difference between them, being the depth of the Ti-Mo system greater than that presented by Ti-Cr, this due to the phenomenon of multiple reflections by Mo (BOLEY *et al.*, 2015), because it has a higher reflectivity coefficient than chrome, this phenomenon also explained in Section 4.2.

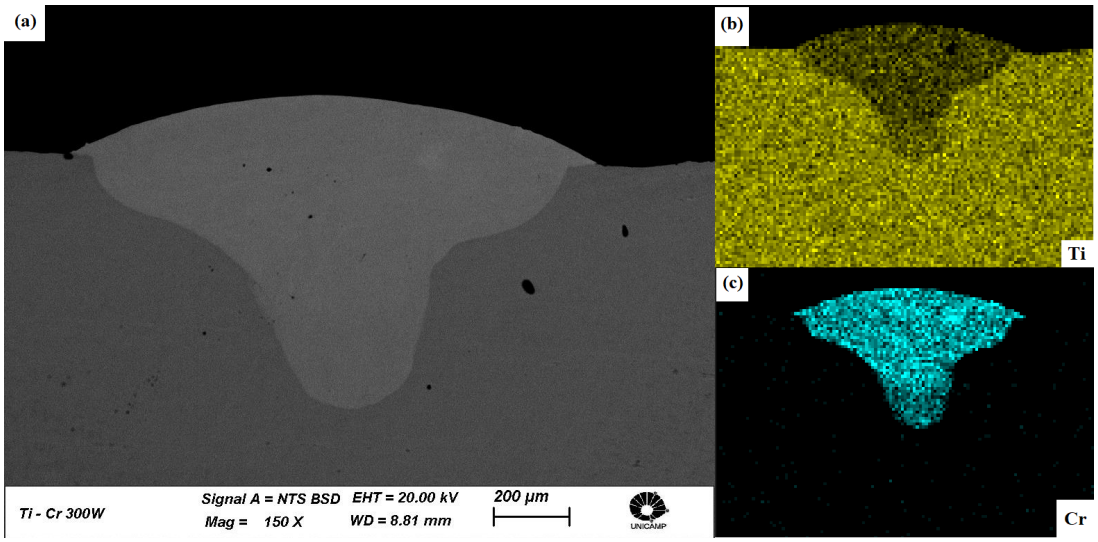

Figure 4.20 – EDS map analysis of TI-Cr single laser track 300 W laser power. Ti (b) yellow, and Cr (c) cyan.

Based on EDS mapping, as shown in Figure 4.20, we know that Ti is observed in yellow (b), and Cr is visible in cyan (c). Unlike the previous powers (150 W and 200 W) presented in sections 4.2 and 4.3, in this case, the distribution of Ti and Cr in the fusion zone is homogeneous; in addition to the formation of the fusion zone, no apparent changes are observed in the microstructure and distribution of the elements along it. The increase of the power up to 300 W allows better absorption of the energy emitted by the laser. However, the keyhole fusion zone shape (KIM *et al.*, 1995) is not optimal for surface treatment since it provides the element that makes this modification penetrate more into the substrate, changing the expected properties and leaving a high concentration of substrate on the surface of the fusion zone.

In Figure 4.21, we can observe the EDS map analysis when we can see the distribution of Mo in the Ti substrate using a laser power of 300 W.

It is detailed that in the upper zone of the fusion zone, there are spaces in which Mo unmelted particles is presented, especially in the upper left site and in the center of the fusion

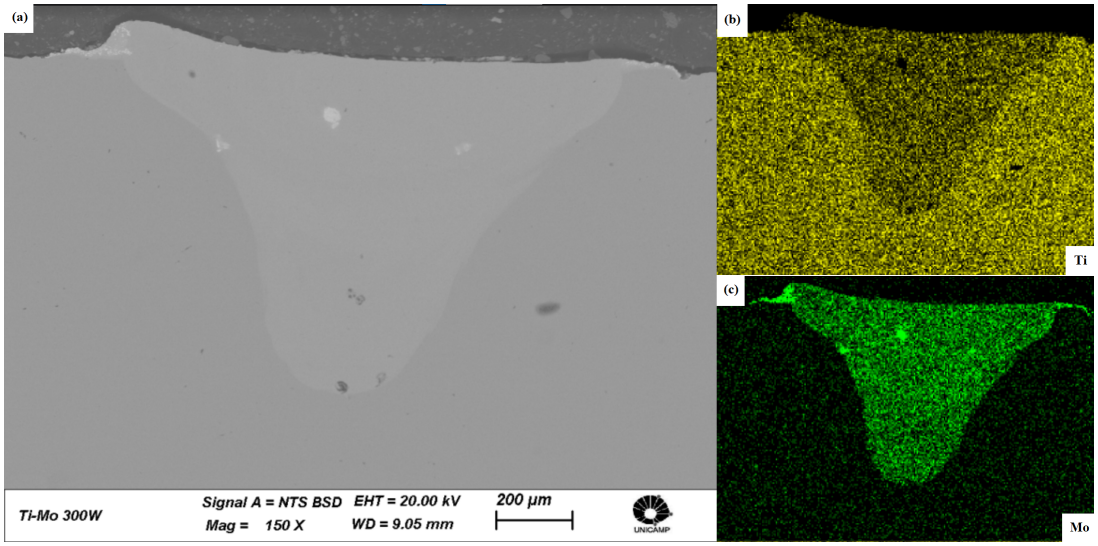

Figure 4.21 – EDS map analysis of TI-Mo single laser track 300 W laser power. Ti (b) yellow, and Mo (c) green.

zone where the laser performed the treatment. We also observe that when comparing Figure 4.20 (b) with Figure 4.21 (b), Ti has a significant concentration in the fusion zone where the substrate was treated with Mo.

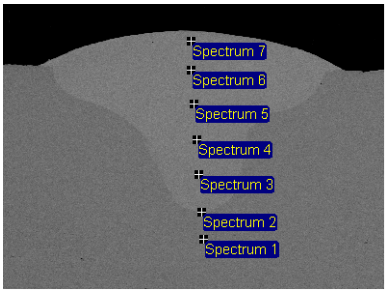

Spectrum	Ti	Cr
Spectrum 1	100	0
Spectrum 2	100	0
Spectrum 3	77.0	23.0
Spectrum 4	64.4	35.6

Spectrum	Ti	Cr
Spectrum 5	66.9	33.1
Spectrum 6	66.3	33.7
Spectrum 7	66.0	34.0

Figure 4.22 – EDS point analysis of Ti-Cr single laser track 300 W laser power. Values in weight percent.

Besides performing EDS analysis in mapping mode, we also conducted a point EDS analysis for the Ti-Cr single laser track, depicted in Figure 4.22. We measured from the substrate to the surface of the fusion zone. We can see that at the bottom of the fusion zone, and the Cr concentration is lower (spectrum 3, Figure 4.22), there is also a significant change between Spectrum 3 and 4. However, above Spectrum 4, there is no considerable change in the ratio and concentration of both elements. Also, we can notice a decrease in Cr concentration concerning the spectra presented in Figure 4.11 for the Ti-Cr system treated with a laser power of 150 W and in Figure 4.17 for the same system treated with a higher power (200 W).

The Ti-Mo system (Figure 4.23) has a similar behavior to the Ti-Cr system (Figure 4.22),

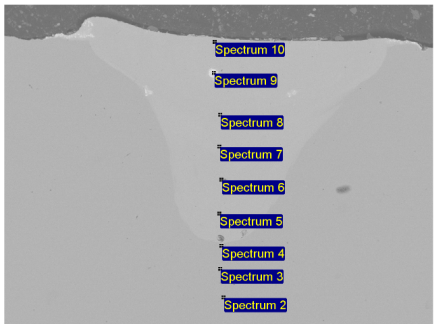

Spectrum	Ti	Mo
Spectrum 2	100	0
Spectrum 3	100	0
Spectrum 4	100	0
Spectrum 5	91.3	8.7
Spectrum 6	92.4	7.6

Spectrum	Ti	Mo
Spectrum 7	90.5	9.5
Spectrum 8	90.4	9.6
Spectrum 9	22.0	78.0
Spectrum 10	90.0	10.0

Figure 4.23 – EDS point analysis of Ti-Mo single laser track 300 W laser power. Values in weight percent.

where there is a variation between the bottom of the fusion zone and the surface of the area treated with the laser. The multiple reflection phenomenon makes the fusion zone deeper due to the high absorption of energy coming from the laser, compared to the Ti-Cr system; where we can observe, compared to the information obtained for other laser powers, 150 W (see Figure 4.12) and 200 W (see Figure 4.18), that the Mo dilution in the fusion zone increased for the surface treatment with 300 W laser power.

4.4.1 Ti-Cr 300 W interface microstructure between fusion zone and substrate

Approaching the interface between Ti and Cr, as shown in Figure 4.24, a microsegregation of the Ti-Cr mixture towards the Ti substrate can be observed. These microstructures may have been derived from the cooling process at the interface, which could have generated these structures of the present phases for these Cr compositions in Ti.

According to the literature, this may be due to the presence of two phases, α-Ti and β-Ti(Cr). We found no significant differences or distinguishable phases in the Ti-Mo single laser track regarding interface broadening.

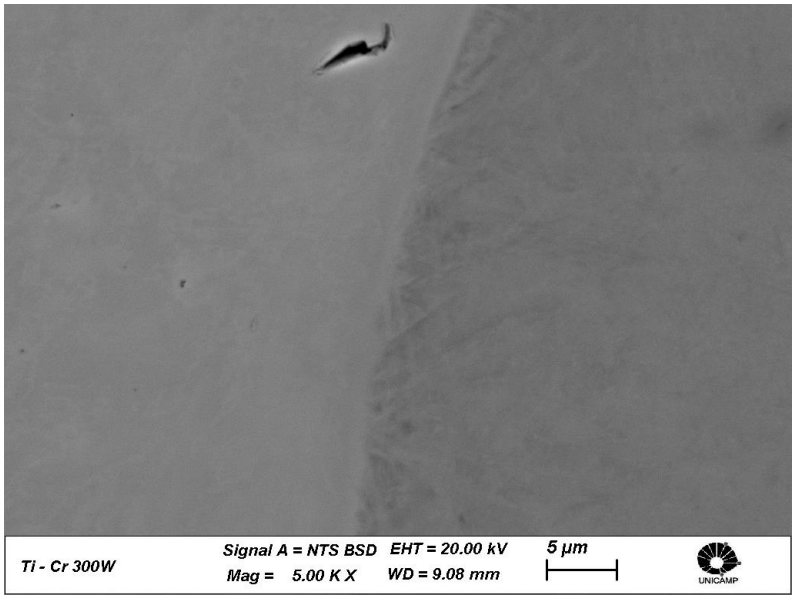

Figure 4.24 – Ti-Cr 300 W interface between fusion zone and substrate.

4.5 Ti-Cr, and Ti-Mo 450 W single laser track.

Finally, a single laser track was manufactured where the laser power was increased to 450 W. After manufacturing the part, the metallography necessary to carry out an analysis by SEM in BSE mode was performed; the result is shown below in Figure 4.25 for the Ti-Cr system (a) and Ti-Mo (b).

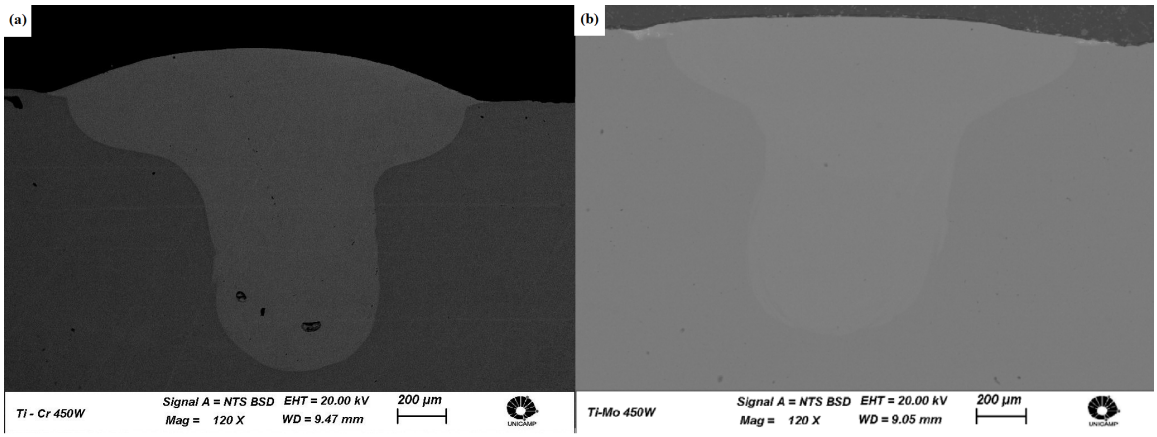

Figure 4.25 – SEM analysis in BSE mode from Ti-Cr (a) and Ti-Mo (b) Fusion zones.

In Figure 4.25 (a), where the Ti-Cr system is shown, the formation of porosities in the lower part of the fusion zone can be appreciated, in addition to a precise shape in Keyhole due to the high power used for the elaboration of this single laser track. In the same way, the Ti-Mo (Figure 4.25 (b)) system presents the shape; it also intuited a high dilution of Mo in the

Ti substrate because although Mo has a higher molecular mass and in the analysis by BSE, it should be differentiated in the piece concerning Ti, we see a slight differentiation between both elements. But, unfortunately, it isn't easy to distinguish them.

Table 4.6 shows the dimensions of the fusion zone of each of the systems, having a similarity between both fusion zones.

Table 4.6 – Width and depth of the Ti-Cr and Ti-Mo fusion zones using 450 W of laser power.

Sample 450 W	**Width (μm)**	**Depth (μm)**
Ti - Cr	1708	1136
Ti - Mo	1653	1198

Both the width and depth increased with the increase of the laser power. However, in the case of Ti-Cr, the depth had a more significant increase compared to the rise in the depth by the Ti-Mo system, concerning the data in Table 4.5, where the power used was 300 W. In the same way, as for the previous powers, an EDS analysis was performed in map mode to see the distribution of the elements in the piece.

In Figure 4.26, this distribution can be seen for the Ti-Cr system, where a greater intensity of Ti (yellow, Figure 4.26 (b)) can be seen, which indicates a higher dilution of this in the fusion zone, as can be seen in Figure 4.26 (c), Cr (cyan) where a complete distribution can be seen in the fusion zone. Unlike other powers, there is no considerable concentration of Cr along the fusion zone, nor the evidence of phenomena present for lower powers.

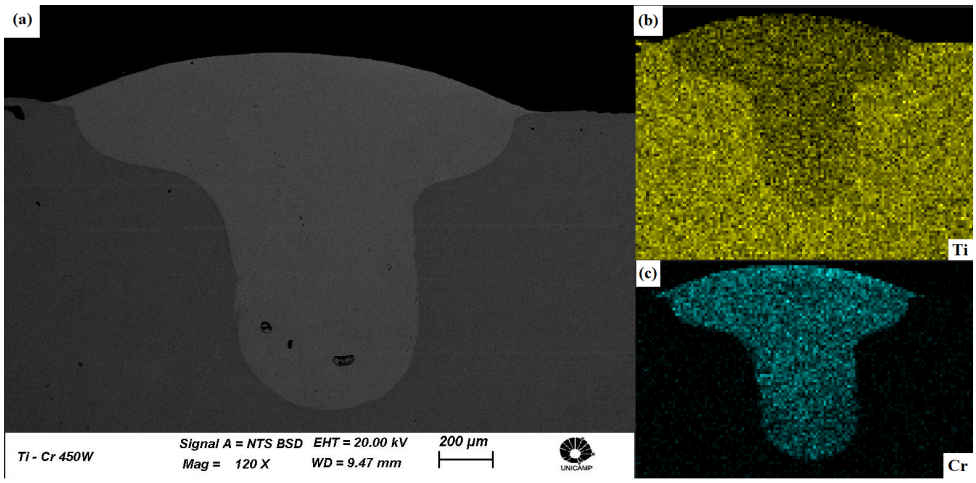

Figure 4.26 – EDS map analysis of TI-Cr single laser track 450 W laser power. Ti (b) yellow, and Cr (c) cyan.

Figure 4.27 shows, on the other hand, the EDS map analysis of the Ti-Mo system. The Ti

shown in yellow (Figure 4.27 (b)) presents a uniform distribution along the fusion zone; from the intensity of the color, it can be intuited that it has a high concentration along the area affected by the laser treatment. In the same way, it can be seen in Figure 4.27 (c) that Mo (green) has a more uniform distribution along the single laser track, compared to the images of previous powers. In addition to the color intensity for this power is lower, which may indicate a lower concentration of Mo in this test.

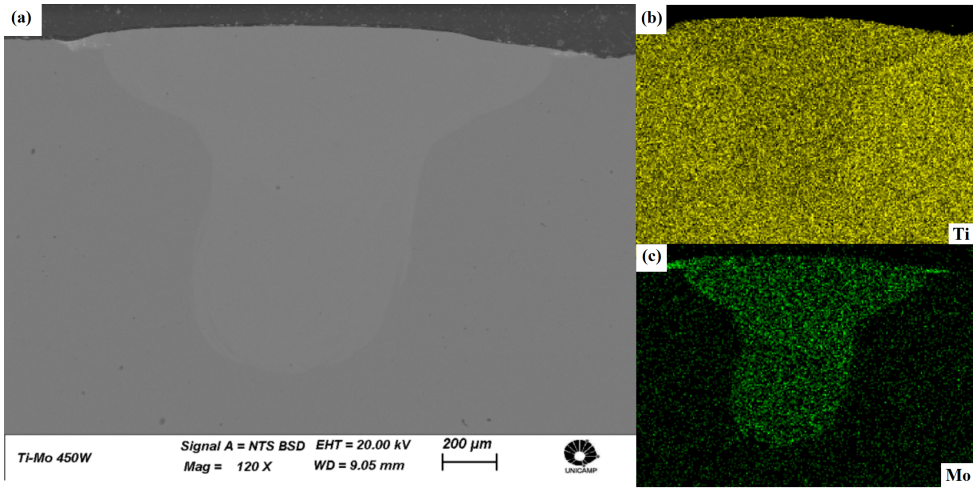

Figure 4.27 – EDS map analysis of TI-Mo single laser track 450 W laser power. Ti (b) yellow, and Mo (c) green.

Finally, in order to guarantee a complete evaluation of the concentration of the elements in the single laser track, an EDS point analysis was performed to obtain a quantitative value of the distribution of Ti, Cr, and Mo along the fusion zone. Initially, it is shown in Figure 4.28 that Cr presents a uniform distribution along the fusion zone, also obtaining an increase in the value of Cr as it approaches the surface of the single laser track; an approximate increase of 15 % in weight percentage can be appreciated from this analysis. Additionally, a decrease in Cr concentration for that obtained with the immediately preceding power (Figure 4.22, 300 W) of approximately 50% is observed.

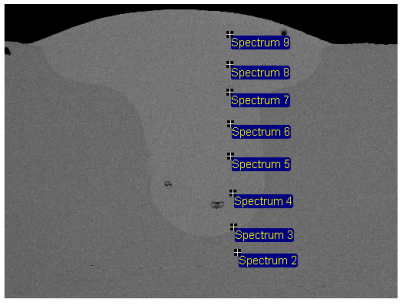

Spectrum	Ti	Cr
Spectrum 2	100	0
Spectrum 3	88.6	11.4
Spectrum 4	86.2	13.8
Spectrum 5	85.1	14.9

Spectrum	Ti	Cr
Spectrum 6	80.5	19.5
Spectrum 7	80.7	19.3
Spectrum 8	79.3	20.7
Spectrum 9	74.9	25.1

Figure 4.28 – EDS point analysis of Ti-Cr single laser track 450 W laser power. Values in weight percent.

On the other hand, for the Ti-Mo system there is a greater dilution of Mo in the fusion zone, as is presented in Figure 4.29; we can see on average, a concentration of approximately 6%, this in contrast with the perceived color intensity in Figure 4.23, where a considerable increase of the Mo diffusion in the Ti substrate is seen (Figure 4.27).

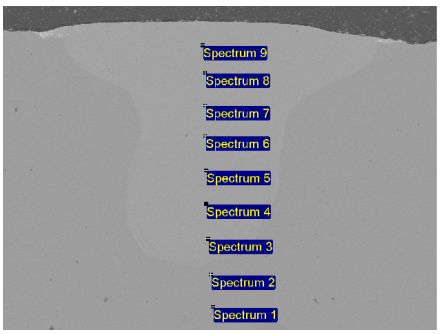

Spectrum	Ti	Mo
Spectrum 1	100	0
Spectrum 2	100	0
Spectrum 3	95.3	4.7
Spectrum 4	95.3	4.7
Spectrum 5	95.0	5.0

Spectrum	Ti	Mo
Spectrum 6	93.5	6.5
Spectrum 7	93.9	6.1
Spectrum 8	94.7	5.3
Spectrum 9	94.1	5.9

Figure 4.29 – EDS point analysis of Ti-Mo single laser track 450 W laser power. Values in weight percent.

Figure 4.30 shows a close-up of the single laser track interface fabricated with 450 W laser power from the Ti-Cr system, where no detailed microstructures or different phases are observed.

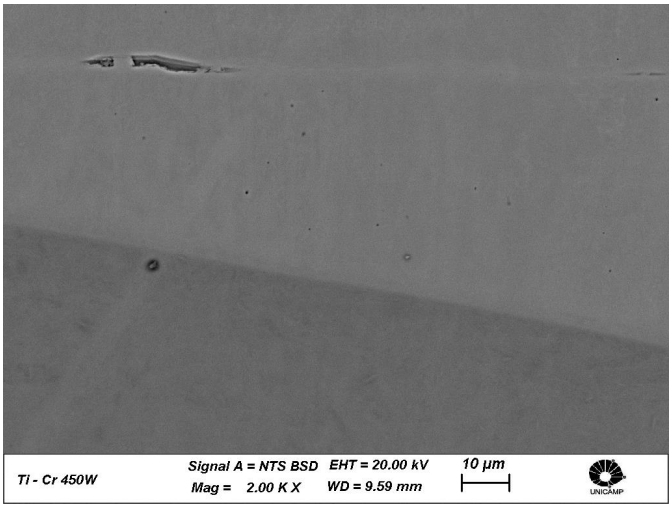

Figure 4.30 – Ti-Cr 450 W interface between substrate and fusion zone.

4.6 Concentration, width and depth fusion zone dependence on laser power

By elaborating a graphical summary of the results obtained in the single laser tracks fabricated at different laser powers, Figure 4.31 and Figure 4.31, compares the measurements made for the width and depth of the fusion zone for each of the single laser tracks fabricated and analysed in the previous sections. For the width, comparing each of the elements, we have in Figure 4.31 a similarity in the measurements between Mo (green) and Cr (blue), even having differences in the formation of the fusion zone, a similar increase is maintained for each of these as the laser power is increased.

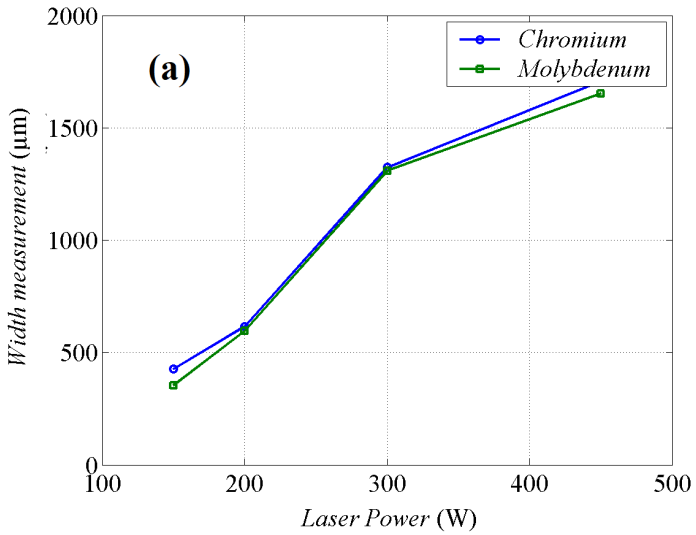

Figure 4.31 – Comparison between Cr and Mo width fusion zone width concerning power variation (W).

As in Figure 4.31 (a), in Figure 4.32 (b) the depth of the fusion zone is compared, finding that in this case, the depths present for the Cr single laser track are less than for Mo, and like the width, there is also an increase in the measurement as the laser power is increased. Taking into account what was explained above about the effect of multiple reflections (LEVA, 2016; BOLEY *et al.*, 2015), we can also say that this phenomenon inside in the measurement of the depth of the fusion zone, having a better transmission of energy between Mo to Ti substrate than from Cr to Ti substrate; generating more fusion of the Ti substrate and making deeper the fusion zone. Therefore, a greater depth is observed comparing the single laser track of Mo (green) and Cr (blue).

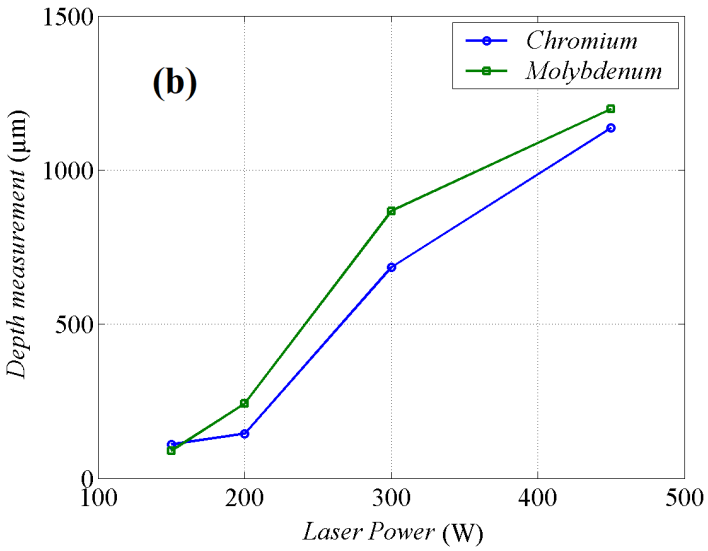

Figure 4.32 – Comparison between Cr and Mo fusion zone depth concerning power variation (W).

At the same way for width and depth, Figure 4.33 shows the variation of the average Cr and Mo concentrations in the fusion zone concerning the power variation. the data in Figure 4.33 is an average of the concentrations obtained in the EDS point analysis.

Analyzing each of the elements, we have that for Cr (blue), the decrease in the concentration of this element found in the fusion zone descends abruptly from the power 150 W to 300 W, and between the last two powers (300 W, 450 W). However, the increase in power is 50%, and the decrease in concentration is lower in percentage. On the other hand, Mo (green) presents a higher dilution in the Ti substrate, making it concentration lower for each of the points compared to the Cr concentrations.

A comparison between the points in Figure 4.33 for each element, we have that Cr, for each of the powers, has a higher concentration in the fusion zone concerning the data obtained

for Mo. According to Leva (2016) and Boley *et al.* (2015), as mentioned previously in Section 4.2, although the elements have a high reflectivity coefficient, the effect of multiple reflections causes this high reflectivity to be transformed into a more remarkable ability to absorb laser energy by the Ti substrate, because the angle of reflectivity and the shape of the each of the powders, makes it more likely to enter a neighboring particle and the laser energy transfer is more effective within the same material; until finally reaching the substrate, causing, in turn, a deeper fusion zone and high dilution in Mo concentration than Cr; since Ti has a lower reflectivity coefficient, it will therefore absorb more energy from laser in Ti-Mo system.

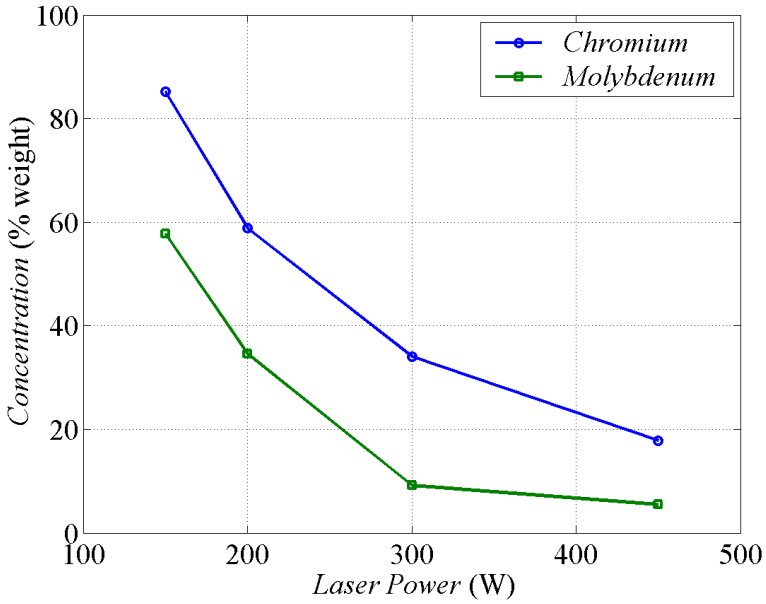

Figure 4.33 – Comparison between Cr and Mo concentrations (weight percent) concerning power variation (W).

4.7 Ti-Cr and Ti-Mo coatings

In addition, to performing the single laser track for each of the materials, two additional tests were performed to verify the compatibility between the two elements in their respective systems: Ti-Cr and Ti-Mo. First, coatings were performed with the use of the laser in a continuous way, following a constant path of approximately 10 mm in the X axis and then in the Y axis of 0.2 mm, thus tracing a consistent approach that finally allowed to have a coating of approximately 10 mm by 5 mm. For both systems, it was performed for one layer and two layers, at the same power of 300 W, this power was chosen due to the results of the single laser track for Mo in particular.

4.7.1 One layer coating

For these tests, the own-designed equipment was used to fabricate one layer of each element on their respective Ti substrate using 0.25 mm thickness of each powder; Figure 3.2 (b) show the pre-placed powder on the substrate; they were then laser treated at 300 W power. Figure 4.34 shows SEM images in BSE mode for each system.

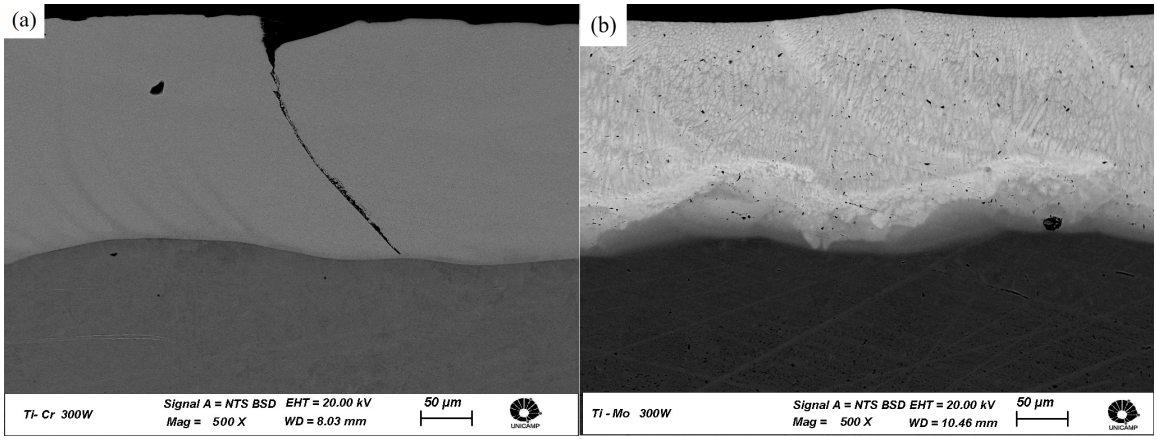

Figure 4.34 – Ti-Cr (a) and Ti-Mo (b) systems coating Ti substrate. Laser power 300 W.

The Ti-Mo system presented in Figure 4.34 (b) shows an appreciable separation between the distances of the beginning and midpoint of the fusion zone, indicating an overlap between the laser tracks that allows a constant coating along the sample (CARVALHO *et al.*, 2018; LEVA, 2016). In the same way, a brighter can be observed for compositions richer in Mo, as well as the existence of microstructures of the Mo coating, which contains dendrites in the fusion zones and micro-segregation in the interface zone.

On the other hand, we can observe the Ti-Cr system in Figure 4.34 (a), where, contrary to the Ti-Mo system, it does not present apparent differentiation in the microstructure; however, it can be appreciated that it has fracture that is along of the coating. In the same way, there is differentiation between the laser tracks, and assuming a homogeneous solution formation at the time of fusion.

Similarly to analyzing the single laser track, we used EDS mapping better to understand the surface element distribution in the samples. For example, Figure 4.35 shows the distribution for Ti (yellow) (b) and Cr (cyan) (c), where it can be observed that Cr does not present microsegregation towards the substrate and that there is a homogeneous mixture between Ti and Cr (a) and Cr (b).

Figure 4.36 shows the EDS map of the Ti-Mo system, which was coated using a laser

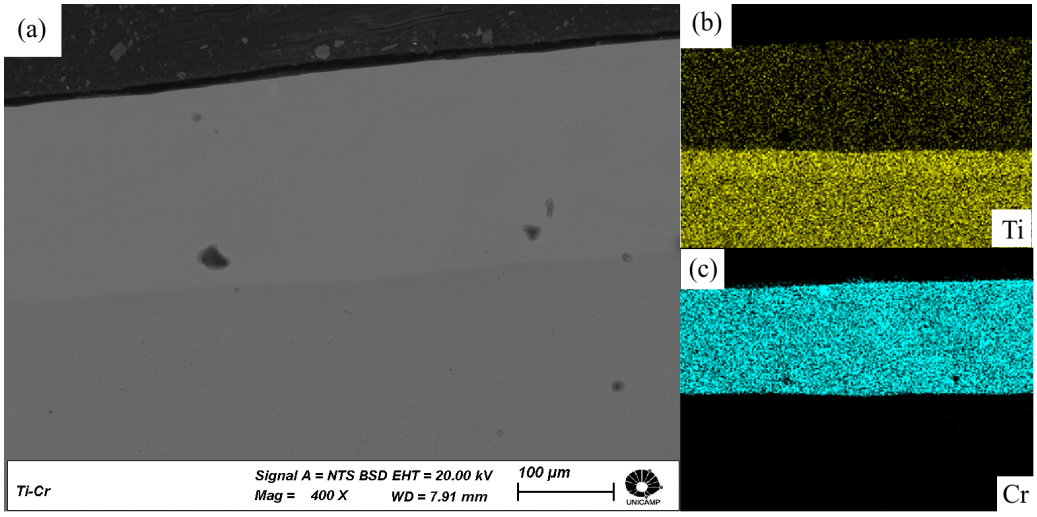

Figure 4.35 – EDS map Ti-Cr coating, Ti (yellow) (b) and Cr (cyan) (c)

power of 300 W and a layer thickness of 0.25 mm. Similar to the Ti-Cr system, the EDS map demonstrates good integration of Mo in Ti with the color intensity.

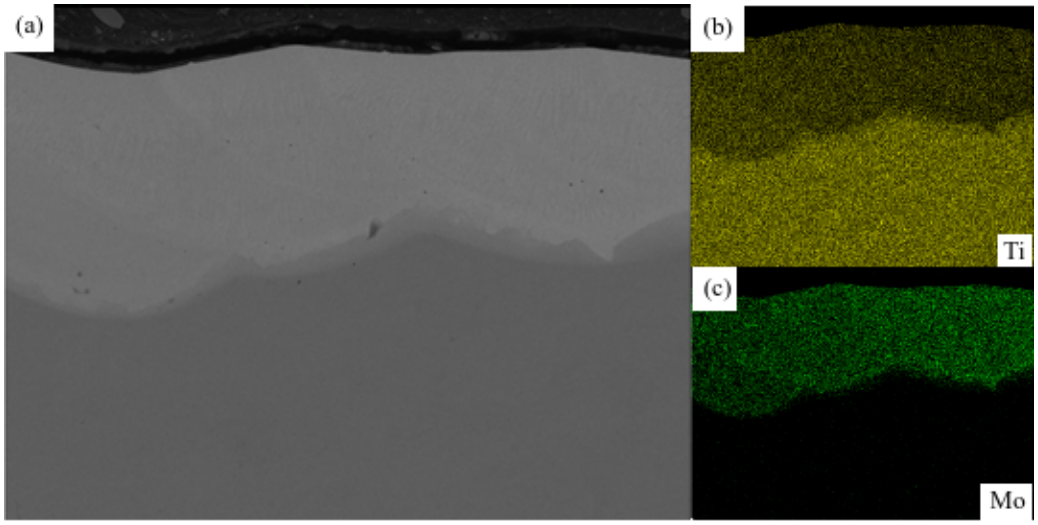

Figure 4.36 – EDS map Ti-Mo coating, Ti (yellow) (b) and Mo (green) (c)

In addition to generating an EDS map, we conducted a EDS point analysis along the test bodies to understand the distribution of each element across the fusion zone. Figure 4.37 displays the concentration of Cr and Ti, which shows the distribution from the substrate to the sample's surface.

As in the section 4.4, we can observe in Figure 4.37 a uniform distribution along the area between the interface and the surface of the sample. Moreover, comparing the results with those obtained in the Figure 4.22, we observe no significant changes in the concentration of Cr in the fusion zone that was approximately 35% weight percent in Cr in both cases.

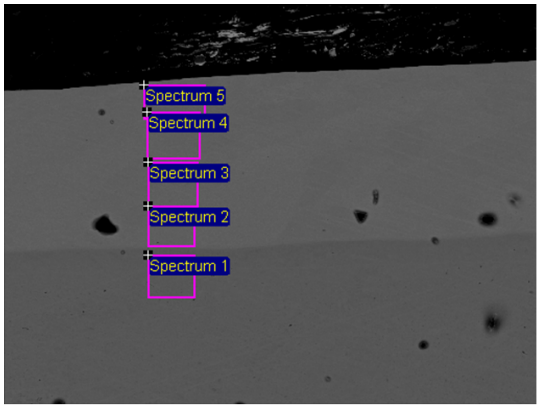

Spectrum	Ti	Cr
Spectrum 1	100	0
Spectrum 2	65.7	34.3
Spectrum 3	64.3	35.7
Spectrum 4	64.3	35.7
Spectrum 5	61.1	38.9

Figure 4.37 – EDS point analysis from Ti-Cr coating sample.

On the other hand, in Figure 4.38, we observe an increase in the concentration of Mo in the fusion zone (29%), which higher that the concentration obtained in the single laser track manufactured and analyzed in the Section 4.4 that was approximately 9%.We presume that such an increase may be due to the overlap of the laser pass fusion zones, causing an increase in absorption laser energy by Mo and the unfused particles that we observed in the Figure 4.21 fusion zone, were melted and distributed along the coating.

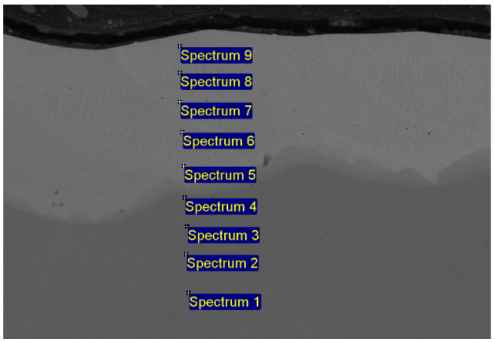

Spectrum	Ti	Mo
Spectrum 1	100	0
Spectrum 2	100	0
Spectrum 3	100	0
Spectrum 4	100	0
Spectrum 5	72.6	27.4

Spectrum	Ti	Mo
Spectrum 6	71.1	28.9
Spectrum 7	70.6	29.4
Spectrum 8	71.0	29.0
Spectrum 9	70.8	29.2

Figure 4.38 – EDS point analysis from Ti-Mo coating sample.

4.7.2 Dual layer Ti-Cr and Ti-Mo coating

Finally, we used our own-design equipment to separately fabricate two test specimens treated with laser in the same way as in section 4.7.1. However, an additional layer of the same material was added, changing the direction the laser travels for the second layer. We automatically programmed the movement in the Y-axis and then in the X-axis to simulate the laser movement when used in PBF additive manufacturing equipment. Figure 4.39 displays the results for both 2-layer coating systems presented through BSE mode SEM analysis.

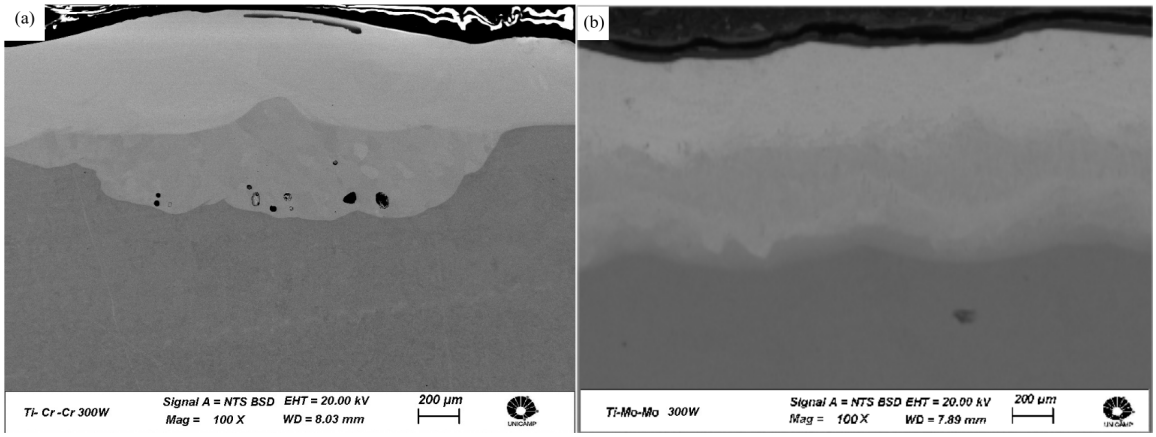

Figure 4.39 – SEM images from dual layer test Ti-Cr (a) and Ti-Mo (b) systems.

The results of the SEM analysis in the BSE mode of the worked systems show a semi-uniform distribution for both. In Figure 4.39 (a), for the Ti-Cr system, a differentiation between the two layers of added Cr is observed; also, the formation of porosity at the bottom of the first layer, near the interface, possibly because during the process, metal powder is vaporized using a laser; then is rapidly solidified, and it can become trapped within the solidifying metal and cause porosity.

In the same way as the Ti-Cr system, Figure 4.39 (b) also shows a difference in layer intensity, indicating a higher concentration of one of the elements for the lower layer. However, unlike Ti-Cr, Ti-Mo does not exhibit porosity in the area observed in the SEM analysis and presents a better distribution of Mo in the coating. To better understand the element distribution, we conducted an EDS analysis in mapping mode to verify it.

The EDS analysis in SEM was used to obtain the Ti (yellow), and Cr (cyan) element map, as shown in Figure 4.40. The color intensity variation is observed in each layer of the laser surface treatment. The layer with porosity has a lower amount of Cr and a moderate amount of Ti. As we move up to the second layer, the intensity of both elements changes, increasing for Cr and decreasing for Ti. We performed a EDS point analysis to obtain a quantitative distribution of these elements, and the result is shown in Figure 4.42.

As with the Ti-Cr system, Figure 4.41 shows the distribution of the Ti (yellow) and Mo (green) elements used to fabricate the two-layer Mo coating. Compared with Figure 4.40 of the Ti-Cr system, a better dispersion of the components can be observed throughout the coating, and a better distribution of the layers along the substrate surface infers a better coating. There is also a difference in color intensity, indicating a higher concentration of Mo in the surface layer,

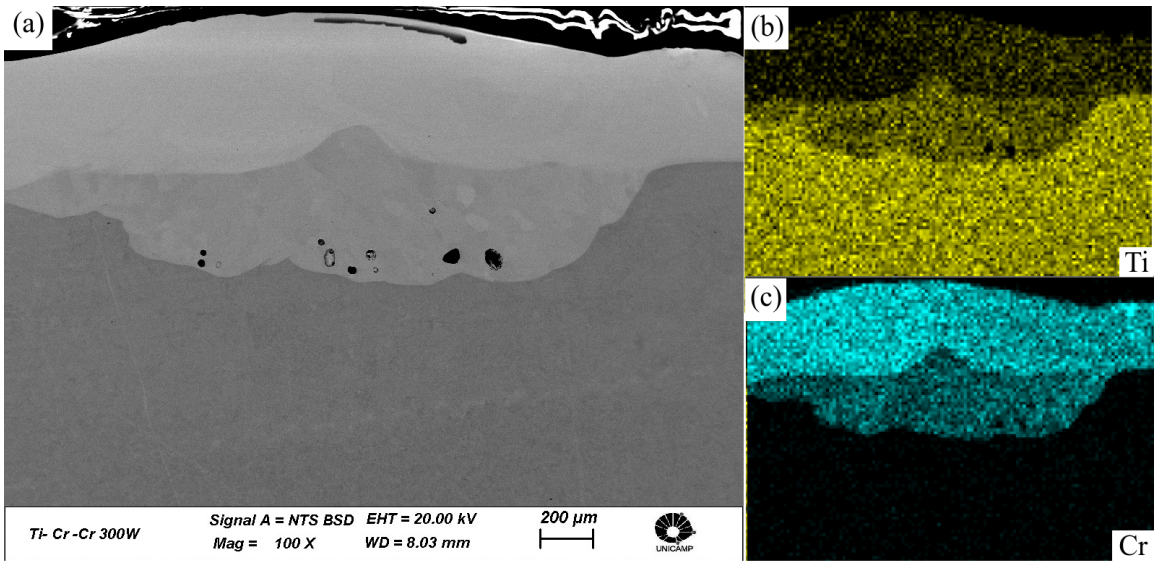

Figure 4.40 – EDS map from Ti-Cr dual layer system.

while Ti predominates in the intermediate layer. As with the Ti-Cr system, a EDS point analysis was performed to gain insight into the distribution of the elements.

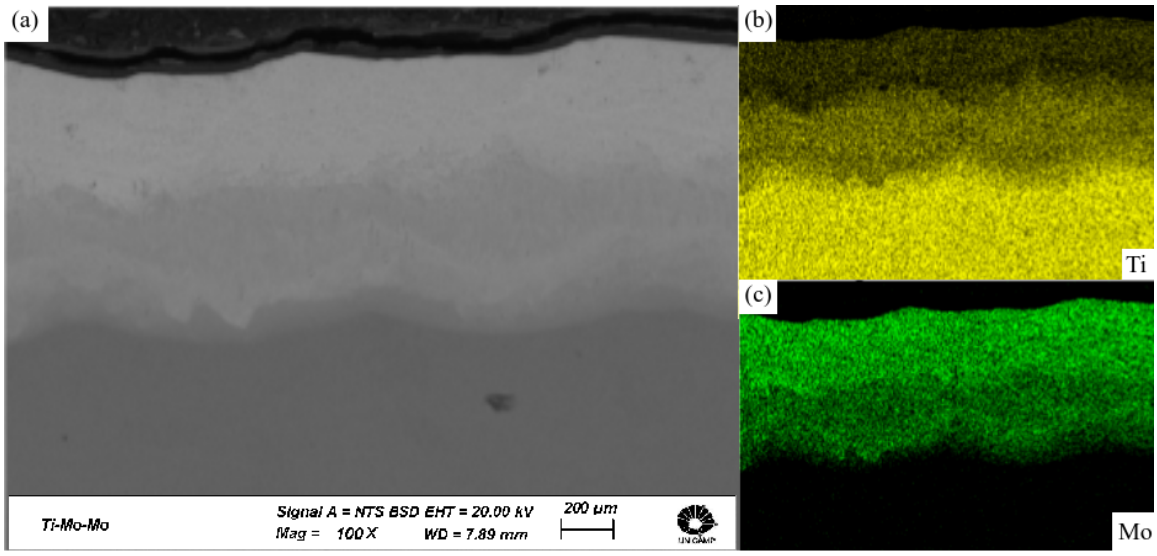

Figure 4.41 – EDS map from Ti-Mo dual layer system.

Figure 4.42 shows a point analysis obtained by EDS, which confirms that there is a change in the concentrations of Ti and Cr presented in Figure 4.40 throughout the two layers; it can be observed that the concentration of Cr increases by almost 90% between the first and second layers, indicating a significant separation between the two layers. On the other hand, as it approaches the modified surface, a decrease in the concentration of Ti is observed in each layer due to the dilution of Ti caused by the increase in Cr concentration when an additional layer is

added.

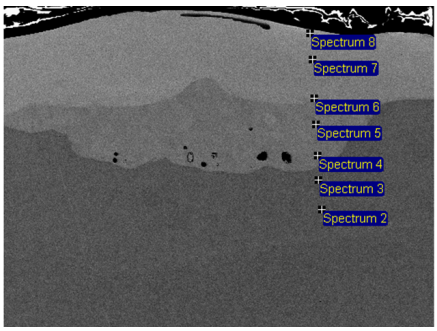

Spectrum	Ti	Cr
Spectrum 2	100	0
Spectrum 3	100	0
Spectrum 4	71.9	28.1
Spectrum 5	71.8	28.2

Spectrum	Ti	Cr
Spectrum 6	54.0	46.0
Spectrum 7	56.0	44.0
Spectrum 8	54.6	45.4

Figure 4.42 – EDS point analysis of Ti-Cr dual layer coating. Values in weight percent.

The EDS point analysis performed on the Ti piece coated with two layers of Mo, whose results are presented in Figure 4.43, shows that, unlike the Ti-Cr system, we can see a constant change in Mo concentrations along the layers. In contrast, in the Ti-Cr system, the difference is more abrupt. Although differentiation between the two Mo layers can also be observed, the constant increase in concentration may indicate that their properties change in a gradient form, as presented in Leva (2016) doctoral thesis.

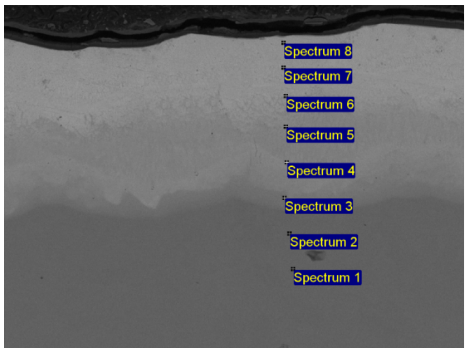

Spectrum	Ti	Mo
Spectrum 1	100	0
Spectrum 2	100	0
Spectrum 3	84.5	15.5
Spectrum 4	59.4	40.6

Spectrum	Ti	Mo
Spectrum 5	62.1	37.9
Spectrum 6	34.8	65.2
Spectrum 7	32.8	67.2
Spectrum 8	29.4	70.6

Figure 4.43 – EDS point analysis of Ti-Mo dual layer coating. Values in weight percent.

4.8 Ti-Mo-Cr system, dissimilar joint between Ti and Cr.

Considering the data presented in the previous sections, we finally proceeded to manufacture the first piece, where the surface of an initial Ti substrate is modified with Mo. After this treatment, a new layer is added by adding Cr powder to the modified Mo surface. After manufacturing the piece, we cut that and subjected it to metallographic treatment for analysis by SEM. The results are presented in Figure 4.44.

The test specimen, was fabricated using a laser power of 300 W for each layer and the change of laser direction strategy was employed, as was used for the fabrication of two-layer

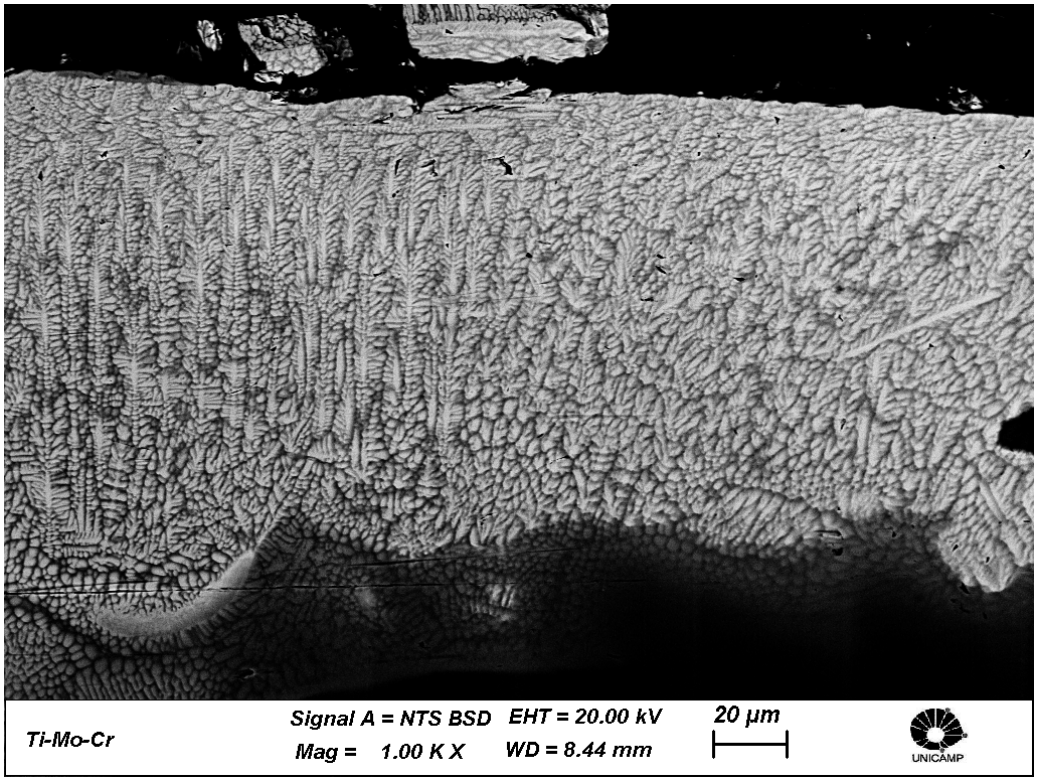

Figure 4.44 – SEM image in BSE mode from Ti-Cr-Mo system.

samples. The pre placed powder layer thickness was maintained at 0.25 mm for each element, and the own-designed equipment presented in Section 3.2 was used.

In Figure 4.44, we can observe the modification made on the surface of Ti, initially with Mo and subsequently with Cr. Both layers were treated with a laser at a power of 300 W. The difference between the microstructures along the modified surface can be noted, with microsegregation and dendritic formations being the predominant microstructures throughout the modified zone. A closer look was taken to detail the microstructures, as shown in Figure 4.45.

Dendritic structures are observed in Figure 4.45 (b) at a magnification of 2.5K. These structures are formed due to the rapid solidification inherent in the additive manufacturing process (DANTZIG; RAPPAZ, 2016). Dendritic structures are brighter, as previously mentioned, as Mo, which has a higher molecular weight than the other two elements, would have a greater presence in these structures. However, the concentration results of these structures are presented in Figures 4.47 and 4.48.

On the other hand, Figure 4.45 (c) shows a micro-segregation, primarily present in the lower part of the modified zone, near the interface with the substrate. This figure corresponds to a 6 K magnification, and it can also be seen how there is a difference between the colorations in the sample. We performed an EDS analysis in map mode to get an idea of the distribution of

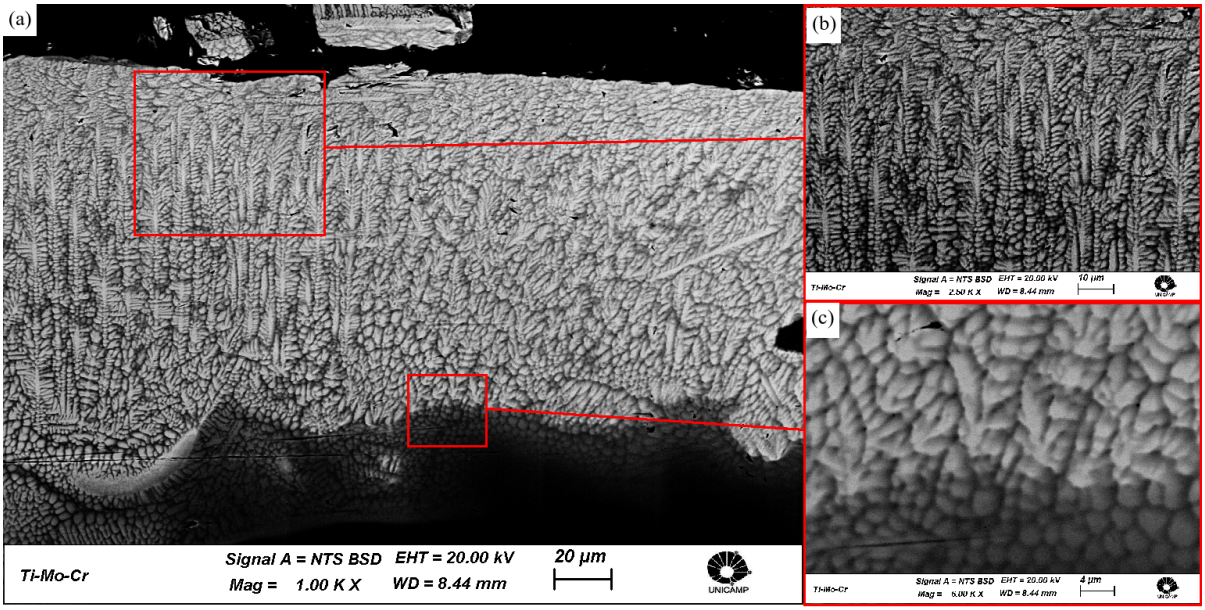

Figure 4.45 – Original (a) and zoomed image by top (b) and down (c) side of modified zone.

the elements in this system, which can be seen in Figure 4.46.

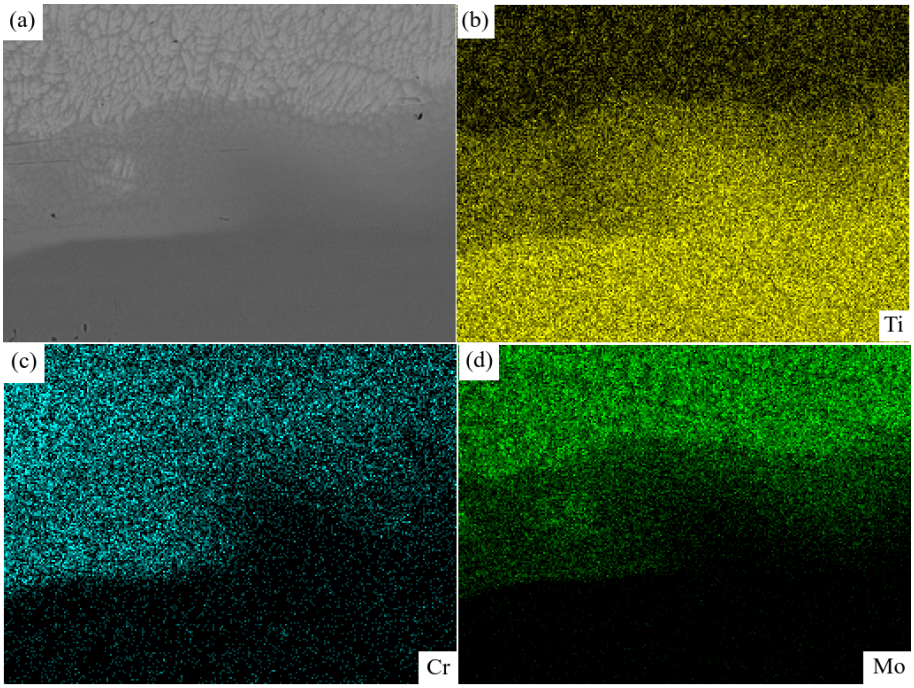

Figure 4.46 – Original (a) and EDS map analysis to Ti (yellow) (b), Cr (cyan) (c), and Mo (green) (d).

The distribution of elements along the coating area can be observed in map mode in Figure 4.46, where Ti (yellow) is present throughout the entire piece but with a decrease in color intensity as it approaches the coating surface. Conversely, Mo (green) reduces color intensity as we move toward the substrate. Meanwhile, Cr (cyan) remains constant until the interface is

closer to the substrate.

Initially, we performed a point analysis by EDS in the structures that present microsegregation which is closer to the Ti substrate; Figure 4.47 shows in spectra 1 and 3 that in the darkest areas of this zone, there is a higher presence of Ti and Cr, while in the brightest ones as in spectrum 2 and 4 are richer in Mo. Additionally, we can observe throughout all the spectrums that the concentration of Ti is high, even though it is noted in spectrum 6 that the dark zone near the interface has a considerably high Ti majority.

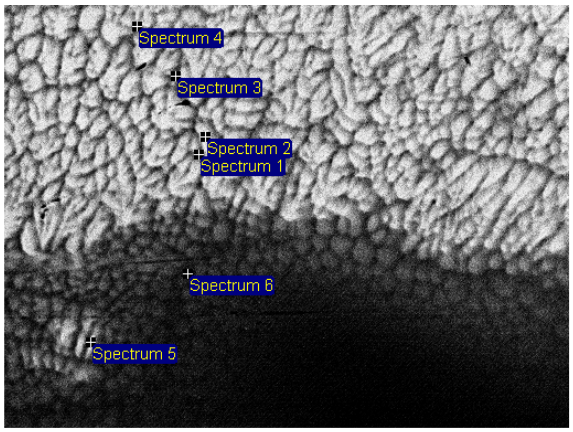

Spectrum	Ti	Cr	Mo
Spectrum 1	58.7	13.2	28.1
Spectrum 2	46.7	6.8	46.5
Spectrum 3	59.3	12.5	28.2
Spectrum 4	54.0	8.5	37.5
Spectrum 5	53.3	8.5	32.2
Spectrum 6	75.5	9.0	15.5

Figure 4.47 – EDS point analysis from Figure 4.45 (c). Values in weight percent.

Finally, we performed an EDS point analysis where dendritic microstructures are predominant, closer to the modified surface area, as done previously for Figure 4.47 (c). Figure 4.48 shows an EDS point analysis from Figure 4.45 (c), where the same phenomenon can be observed.

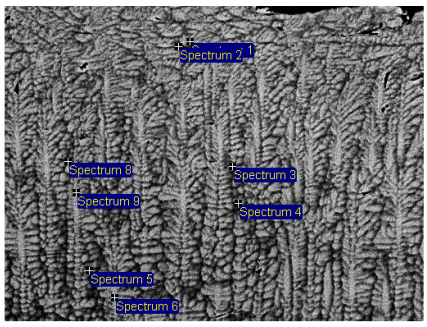

Spectrum	Ti	Cr	Mo
Spectrum 1	46.2	4.9	48.9
Spectrum 2	56.5	9.1	34.4
Spectrum 3	57.2	9.6	33.2
Spectrum 4	46.4	6.3	47.3

Spectrum	Ti	Cr	Mo
Spectrum 5	56.3	17.0	26.7
Spectrum 6	43.1	8.7	48.2
Spectrum 8	55.0	12.1	32.9
Spectrum 9	46.0	7.5	46.5

Figure 4.48 – EDS point analysis from Figure 4.45 (b). Values in weight percent

The brighter areas, such as in spectrum 1, 4, 6, and 9, have a high Mo composition, and these points are situated in the center of the dendrites, confirming that Mo is the first element to solidify due to its high melting point, leading to the growth of dendrites. On the other hand, the

darker areas (spectra 2, 3, 5, and 8) have a high concentration of Ti, and it can be appreciated that the Cr content concerning the weight percent values of the spectra with high Mo content is also considerably higher. Thus, we can assure that in the solidification kinetics, Ti and Cr elements remain in solution, which surrounds the dendrites formed by Mo.

4.8.1 XRD analysis along the sample

The piece initially manufactured with a Mo coating and subsequently with a layer of Cr, mentioned in section 4.8, underwent an XRD analysis. The analysis began at the surface of the sample, then, approximately 50 μm of material was removed by grinding, subtracted from the total height of the sample. Subsequently, after performing the XRD analysis on the new surface of the sample, another 50 μm was removed, and the XRD test was repeated. Finally, four diffractograms were obtained, as shown in Figure 4.49.

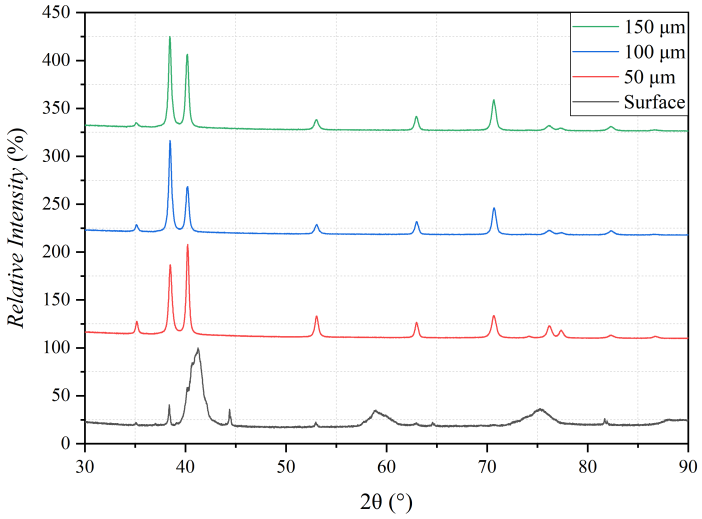

Figure 4.49 – Sample X-ray diffractograms from surface to 150 μm depth, each 50 μm

In Figure 4.49, a similarity can be observed in the diffractograms originating from the sample's interior, while the analysis performed on the surface exhibits a marked difference compared to the others. Therefore, the diffractograms obtained at different depths were grouped and proceeded to be indexed, resulting in the presented results shown in Figure 4.50.

For a better visualization of the identification of the peaks, the 50 μm depth diffractogram is presented, where α-Ti is the unique phase present in the sample (SAILER; MCCARTHY, 1993).

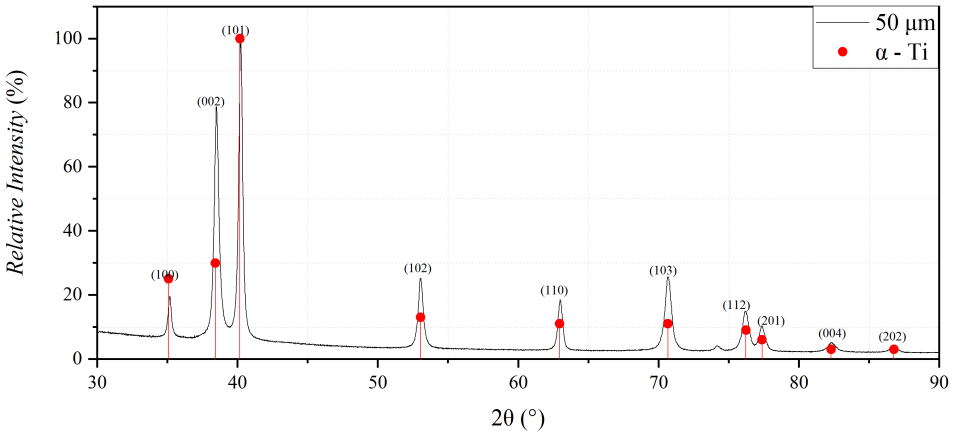

Figure 4.50 – Peaks identification from X-ray diffractogram 50 μm depth.

4.8.1.1 XRD Ti-Mo-Cr from sample surface

The diffractogram obtained from the surface of the piece with the Mo-Cr coating is presented individually in Figure 4.51.

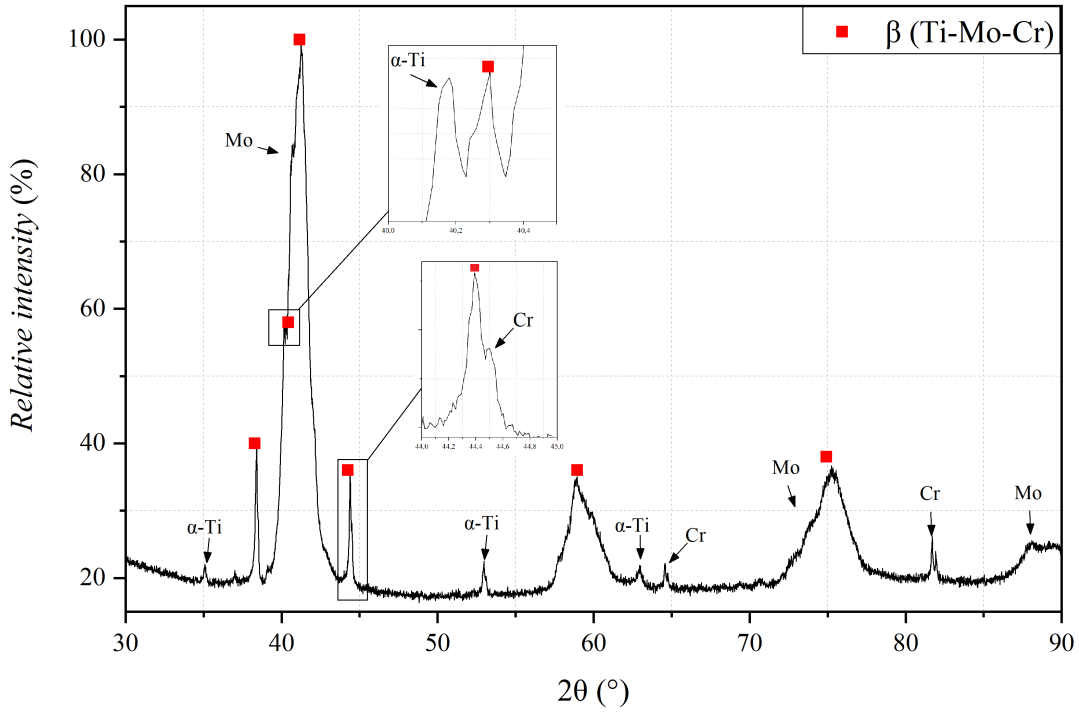

Figure 4.51 – Peaks identification from X-ray diffractogram sample surface.

In addition, Figure 4.51 shows the peaks identification concerning the literature, where it is found that the diffractogram correspond to the BCC microstructure Cr-Mo solid solution (RUDY, 1973). However, the XRD analysis carried out on the surface is displaced approx-

imately 3° due to the presence of Ti; also, peaks correspond to Cr and Mo is presented. In addition to the displacement, broad peaks are observed that are a consequence of roughness in the analyzed surface.

Using the Thermo-Calc simulation software, we can observe in Figure 4.52 that this system in equilibrium presents different phases, such as β-Ti phase (blue). This graph also shows that when cooling begins (liquid line in red), the β-Ti is generated until reaching a temperature of approximately 650°C, where the intermetallic compound $Ti(Cr)_2$ (green) is generated up to room temperature. It is also shown that at temperatures below 360°C, a phase transformation is generated where part of the β-Ti phase becomes α-Ti (magenta). However, at a temperature of 650°C, the system lacks kinetics to generate phase transformations, in this case, the generation of $Ti(Cr)_2$ intermetallic compound and Alpha-Ti phase, since the cooling is rapid inherent to the nature of the technique, leaving a meta-stabilized β phase solution.

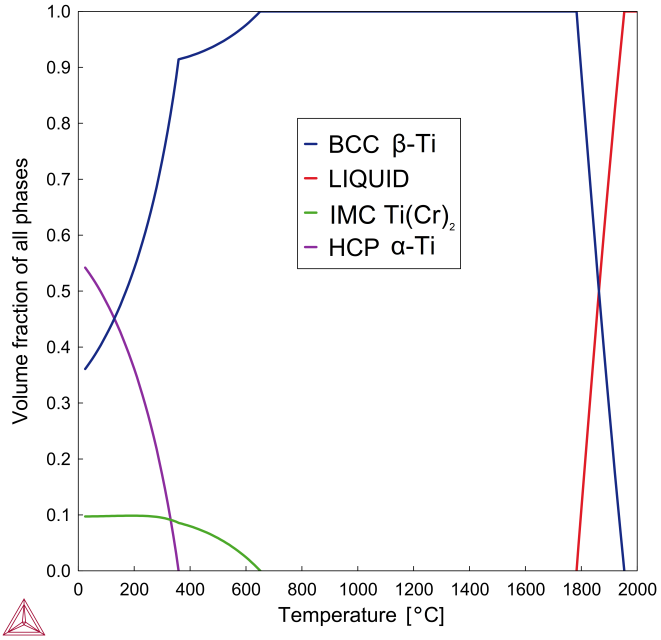

Figure 4.52 – Volume fraction simulation from different phases present in system Ti-Mo-Cr (ANDERSSON *et al.*, 2002).

4.9 Microhardness and instrumented indentation tests

Figure 4.53 shows the indentations performed for microhardness (a) on the surface of the Ti-Mo-Cr system and for instrumented indentation (b) inside the coating.

A instrumented indentation analysis was performed on the Ti-Mo-Cr system sample, varying the distance from the surface to inside 40 μm, until an approximate depth of 200 μm, obtain-

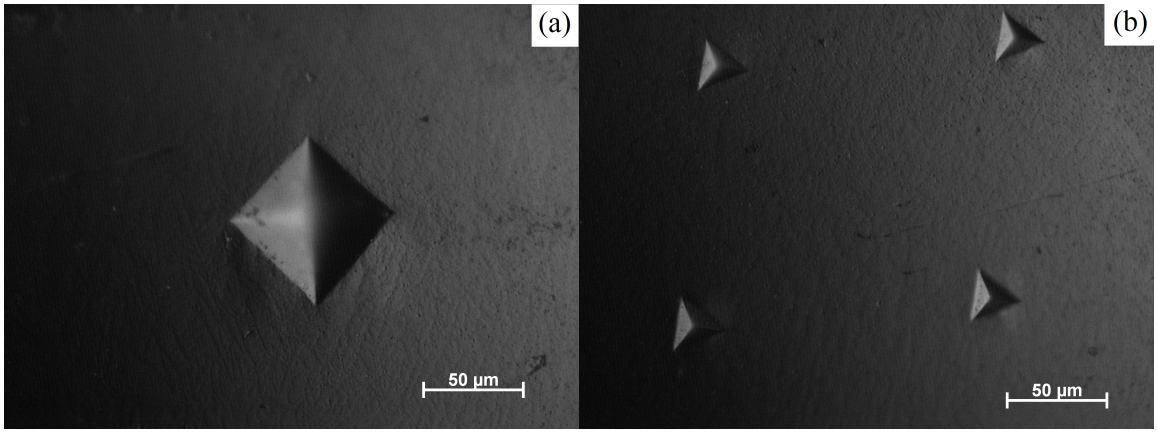

Figure 4.53 – Indentations of microhardness analysis (a) and instrumented indentation analysis (b), performed on the Cr-Mo coating.

ing the results of the hardness and Young's modulus parameters through the modified material that can be seen in Figure 4.54.

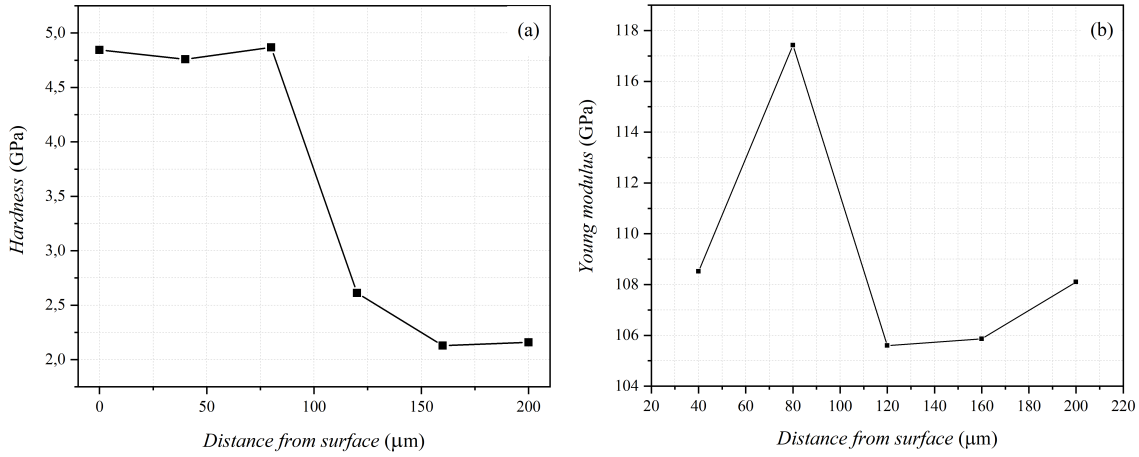

Figure 4.54 – Hardness (GPa) (a), and Young Modulus (GPa)(b) results from Ti-Mo-Cr sample, from surface to substrate.

We can deduce from Figure 4.54 (a) that the hardness is higher in the zone of the material where there is the presence of the three elements until reaching a depth of approximately 80 μm; after 120 μm, a more attenuated decrease is observed, could indicate the absence of Cr in this part of the sample, considering that the increase in the hardness could be due to the β-Ti phase formed by the presence of Mo, since as it was added initially and taking into account what was observed in Section 4.4, part of Mo insidiated in the substrate by the laser power used, in addition to this, it is also observed a decrease in Young's modulus (Figure 4.54 (b)) for the depths 120 μm and 160 μm, compared to the substrate which would be the last point

of both figures, this variation of the increase in hardness with the decrease in Young's modulus was reported by Leva (2016).

4.9.1 Hardness systems comparative

Finally, a comparison of the hardnesses obtained on the surfaces of the Ti-Cr, Ti-Mo, and Ti-Mo-Cr systems was made, as well as a comparison with the one received by the substrate. Figure 4.55 shows the average values of the surface hardnesses measured 15 times in random sites of the surfaces where it was treated with laser. The parts used for these measurements were those analyzed in Section 4.7.1, and the sample was fabricated with the presence of the three elements, which was analyzed in Section 4.8.

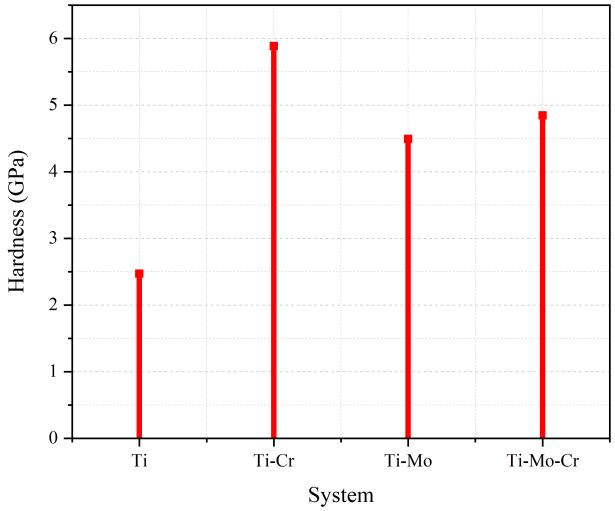

Figure 4.55 – Comparative between surface hardness.

Comparing the hardnesses on the surface concerning the substrate, we can observe that in all cases, it is higher. The Ti-Cr system presents the highest hardness, indicating that the increase in hardness produces embrittlement in this joint and generates the cracks presented at the moment of joining Ti with Cr. However, if an element (Mo) with affinity to those of the initial system (Ti and Cr) is added, the hardness decreases and improves the properties of the joint, making a dissimilar joint viable using an intermediate element.

5 CONCLUSIONS AND RECOMMENDATIONS

The use of own-design equipment that allows reproducing most of the conditions used in the PBF additive manufacturing technique facilitates the use of powder of different particle sizes as well as allows to discard the need for these powdered materials to have a spherical particle shape that allows sliding in the process as requested by some equipment used today. It also allows the use of a smaller amount of material, which reduces the cost of the research, in addition to allowing changes of elements or bonds to carry out compatibility studies between these unions using a laser. Finally, this equipment will enable us to conclude from the research the following points:

(i) By varying the laser power for the Ti-Cr system, we can observe that phenomena such as Marangoni convective flows occur at low laser powers, generating Cr concentration in the corners of the surface of the fusion zone. Also, by using low laser powers such as the 150 W single laser track, fractures are produced in the fusion zone, which indicates fragilization, possibly by intermetallic phases generated at the interface. In the same way, the Ti-Mo system presents an unmelted particles of Mo in the fusion zone, which indicates insufficient energy to perform a complete fusion of the material; however, due to the compatibility between Ti and Mo, it does not present fractures in the interface.

(ii) As the laser power increased, the shape of the fusion zone changed from a conduction shape for the Ti-Cr system with a power of 150 W, passing through a transition-type formation at 200 W and finally arriving at a keyhole-type shape at 450 W laser power, which allowed excellent fusion, thus allowing greater penetration of Cr in the Ti substrate for 300 W laser power. On the other hand, the Ti-Mo system presents a U-shape of the fusion zone for 200 W; for 450 W laser power, a keyhole-type shape is shown, in this case with a greater depth in the fusion zone concerning the Ti-Cr system; this is due to the phenomenon of multiple reflections that allows a better absorption of the laser energy by the substrate since Mo has a higher coefficient than Ti and Cr.

(iii) In addition to the above, observing the EDS analyses carried out at different laser powers; we can see that Mo has lower concentrations in the fusion zone than Cr at all laser powers; at the same time, it presents greater lengths in the fusion zones, which leads to conclude

that Mo presents greater dilution in the fusion zone because a greater amount of Ti substrate is melted compared to the Ti-Cr system. It is also concluded that the concentration of the elements in the fusion zone (in this case, Cr and Mo) depends entirely on the laser power used to perform these procedures, presenting higher concentrations for Cr than for Mo.

(iv) The addition of a Cr layer on a Mo-modified Ti substrate surface generates a Beta metastabilized ternary system, where a solid solution of Cr-Mo and B-Ti phase is presented and where the absence of intermetallic compounds that can be formed between Ti and Cr is also observed.

(v) After performing the hardness analysis for the three coatings, compared with the hardness of the substrate, we can conclude that with the addition of elements separately, a significant increase in hardness is obtained for the Ti-Cr system, which leads us to think that the embrittlement of the interface produces the fractures observed in the analysis by MEV due to the formation of the intermetallic element $TiCr_2$. Following the above, adding Mo as an intermediate element to carry out this surface multicomponent modification considerably reduces the hardness in the layer where the three elements are present. We have that the hardness is reduced by approximately 15%, which allows the viability of this union by reducing the contact between Ti and Cr.

(vi) Finally, the modulus of elasticity of the fabricated part remains approximately constant along the modified zone from the surface to the substrate, presenting a slight increase of roughly 5% when reaching the interface with the pure substrate, thus concluding positively the feasibility of using Mo as an intermediate element to carry out a dissimilar joint between Ti and Cr.

5.1 Suggestions and recommendations.

For future work, the following points are recommended:

(i) It is suggested to increase the number of Mo layers added to the Ti substrate to have a lower presence of the substrate at the interface of the junctions, avoiding the formation of undesired phases altogether.

(ii) Also, to make a smooth transition between the elements by increasing the number of layers per additive manufacturing, thus studying the system as a material with a gradient of functionality, starting from Ti and reaching Cr by varying the concentration of intermediate elements, in this case, Mo.

(iii) To evaluate the biocompatibility of this type of dissimilar joints through cytotoxicity and cell proliferation, evaluating the interface between Mo and Cr.

(iv) Having Cr as the final element of the gasket, it is finally suggested to evaluate the wear and corrosion resistance of the surface.

REFERENCES

AGAPOVICHEV, A.; SOTOV, A.; KOKAREVA, V.; SMELOV, V. Possibilities and limitations of titanium alloy additive manufacturing. In: EDP SCIENCES. **MATEC Web of Conferences**. [S.l.], 2018. v. 224, p. 01064.

ANDERSSON, J.-O.; HELANDER, T.; HÖGLUND, L.; SHI, P.; SUNDMAN, B. Thermo-calc & dictra, computational tools for materials science. **Calphad**, Elsevier, v. 26, n. 2, p. 273–312, 2002.

BOLEY, C.; KHAIRALLAH, S. A.; RUBENCHIK, A. M. Calculation of laser absorption by metal powders in additive manufacturing. **Applied optics**, Optica Publishing Group, v. 54, n. 9, p. 2477–2482, 2015.

BUSCAIL, H.; JACOB, Y.; STROOSNIJDER, M.; CAUDRON, E.; CUEFF, R.; RABASTE, F.; PERRIER, S. X-ray diffraction to study the oxidation mechanism of chromium at elevated temperatures. In: TRANS TECH PUBL. **Materials Science Forum**. [S.l.], 2004. v. 461, p. 93–100.

CAI, Z.; BUNCE, N.; NUNN, M.; OKABE, T. Porcelain adherence to dental cast cp titanium: effects of surface modifications. **Biomaterials**, Elsevier, v. 22, n. 9, p. 979–986, 2001.

CARVALHO, L. R. A. de; SALLICA-LEVA, E.; ENCINAS, E. R.; FOGAGNOLO, J. B. Less-rigid coating in ti obtained by laser surface alloying with nb. **Surface and Coatings Technology**, Elsevier, v. 346, p. 19–28, 2018.

CHOUIRFA, H.; BOULOUSSA, H.; MIGONNEY, V.; FALENTIN-DAUDRÉ, C. Review of titanium surface modification techniques and coatings for antibacterial applications. **Acta biomaterialia**, Elsevier, v. 83, p. 37–54, 2019.

CORIGLIANO, P.; CRUPI, V. Fatigue analysis of ti6al4v/inconel 625 dissimilar welded joints. **Ocean Engineering**, Elsevier, v. 221, p. 108582, 2021.

DANTZIG, J. A.; RAPPAZ, M. **Solidification: -Revised & Expanded**. [S.l.]: EPFL press, 2016.

DONACHIE, M. J. **Titanium: a technical guide**. [S.l.]: ASM international, 2000.

DRAPER, C.; EWING, C. Laser surface alloying: a bibliography. **Journal of materials science**, Springer, v. 19, p. 3815–3825, 1984.

FOGAGNOLO, J. B.; RODRIGUES, A.; LIMA, M. S. F. d.; AMIGÓ, V.; CARAM, R. A novel proposal to manipulate the properties of titanium parts by laser surface alloying. **Scripta Materialia**, Elsevier, v. 68, n. 7, p. 471–474, 2013.

FOGAGNOLO, J. B.; RODRIGUES, A. V.; SALLICA-LEVA, E.; LIMA, M. S.; CARAM, R. Surface stiffness gradient in ti parts obtained by laser surface alloying with cu and nb. **Surface and Coatings Technology**, Elsevier, v. 297, p. 34–42, 2016.

FOX, P.; POGSON, S.; SUTCLIFFE, C.; JONES, E. Interface interactions between porous titanium/tantalum coatings, produced by selective laser melting (slm), on a cobalt–chromium alloy. **Surface and Coatings Technology**, Elsevier, v. 202, n. 20, p. 5001–5007, 2008.

GIRI, S. R.; KHAMARI, B. K.; MOHARANA, B. R. Joining of titanium and stainless steel by using different welding processes: A review. **Materials Today: Proceedings**, Elsevier, 2022.

GUSAROV, A. Radiative transfer, absorption, and reflection by metal powder beds in laser powder-bed processing. **Journal of Quantitative Spectroscopy and Radiative Transfer**, Elsevier, v. 257, p. 107366, 2020.

JOHN, A. A.; JAGANATHAN, S. K.; SUPRIYANTO, E.; MANIKANDAN, A. Surface modification of titanium and its alloys for the enhancement of osseointegration in orthopaedics. **Current Science**, JSTOR, p. 1003–1015, 2016.

JOY, D. C.; ROMIG JR, A. D.; GOLDSTEIN, J.; GOLDSTEIN, J. I. *et al.* **Principles of analytical electron microscopy**. [S.l.]: Springer Science & Business Media, 1986.

KAUR, S.; GHADIRINEJAD, K.; H. OSKOUEI, R. An overview on the tribological performance of titanium alloys with surface modifications for biomedical applications. **Lubricants**, MDPI, v. 7, n. 8, p. 65, 2019.

KAYSSER, W. Surface modifications in aerospace applications. **Surface engineering**, Taylor & Francis, v. 17, n. 4, p. 305–312, 2001.

KHAIRALLAH, S. A.; ANDERSON, A. T.; RUBENCHIK, A.; KING, W. E. Laser powder-bed fusion additive manufacturing: Physics of complex melt flow and formation mechanisms of pores, spatter, and denudation zones. **Acta Materialia**, Elsevier, v. 108, p. 36–45, 2016.

KHAN, M.; DICKENS, P. Selective laser melting (slm) of gold (au). **Rapid Prototyping Journal**, Emerald Group Publishing Limited, 2012.

KIM, J.; WATANABE, T.; YOSHIDA, Y. Effect of the beam-defocusing characteristics on porosity formation in laser welding. **Journal of materials science letters**, Springer, v. 14, p. 1624–1626, 1995.

KURODA, P. A. B.; BUZALAF, M. A. R.; GRANDINI, C. R. Effect of molybdenum on structure, microstructure and mechanical properties of biomedical ti-20zr-mo alloys. **Materials Science and Engineering: C**, Elsevier, v. 67, p. 511–515, 2016.

LEE, M.; LEE, J.; CHOI, Y.; KIM, D.; RHEE, C.; LEE, Y.; HONG, S. Interlayer engineering for dissimilar bonding of titanium to stainless steel. **Materials letters**, Elsevier, v. 64, n. 9, p. 1105–1108, 2010.

LEVA, E. S. Modificação superficial a laser para obtenção de gradientes de dureza e módulo de elasticidade em titânio. **[Thesis] University of Campinas, Campinas/SP, Brazil**, 2016.

LI, W.; KARNATI, S.; KRIEWALL, C.; LIOU, F.; NEWKIRK, J.; TAMINGER, K. M. B.; SEUFZER, W. J. Fabrication and characterization of a functionally graded material from ti-6al-4v to ss316 by laser metal deposition. **Additive Manufacturing**, Elsevier, v. 14, p. 95–104, 2017.

LI, X.; XIE, J.; ZHOU, Y. Effects of oxygen contamination in the argon shielding gas in laser welding of commercially pure titanium thin sheet. **Journal of materials science**, Springer, v. 40, p. 3437–3443, 2005.

LIU, X.; CHU, P. K.; DING, C. Surface modification of titanium, titanium alloys, and related materials for biomedical applications. **Materials Science and Engineering: R: Reports**, Elsevier, v. 47, n. 3-4, p. 49–121, 2004.

MARENZI, G.; IMPERO, F.; SCHERILLO, F.; SAMMARTINO, J. C.; SQUILLACE, A.; SPAGNUOLO, G. Effect of different surface treatments on titanium dental implant micro-morphology. **Materials**, MDPI, v. 12, n. 5, p. 733, 2019.

MOHAN, P.; RAJAK, D. K.; PRUNCU, C. I.; BEHERA, A.; AMIGÓ-BORRÁS, V. *et al.* Influence of β-phase stability in elemental blended ti-mo and ti-mo-zr alloys. **Micron**, Elsevier, v. 142, p. 102992, 2021.

MOLITOR, P.; BARRON, V.; YOUNG, T. Surface treatment of titanium for adhesive bonding to polymer composites: a review. **International Journal of Adhesion and Adhesives**, Elsevier, v. 21, n. 2, p. 129–136, 2001.

MURRAY, J. The cr- ti (chromium-titanium) system. **Bulletin of Alloy Phase Diagrams**, Springer, v. 2, n. 2, p. 174–181, 1981.

MURRAY, J. L. The mo- ti (molybdenum-titanium) system. **Bulletin of Alloy Phase Diagrams**, Springer, v. 2, n. 2, p. 185–192, 1981.

ONUIKE, B.; BANDYOPADHYAY, A. Additive manufacturing of inconel 718–ti6al4v bimetallic structures. **Additive Manufacturing**, Elsevier, v. 22, p. 844–851, 2018.

PANWISAWAS, C.; PERUMAL, B.; WARD, R. M.; TURNER, N.; TURNER, R. P.; BROOKS, J. W.; BASOALTO, H. C. Keyhole formation and thermal fluid flow-induced porosity during laser fusion welding in titanium alloys: Experimental and modelling. **Acta materialia**, Elsevier, v. 126, p. 251–263, 2017.

PEDDIRAJU, V. C.; PULAPAKURA, K. K.; JAGADEESH, D. S.; ATHIRA, K.; GUDUR, S.; SURYAKUMAR, S.; CHATTERJEE, S. Weld deposition of nickel on titanium for surface hardening with ti-ni-based intermetallic compounds. **Materials Today: Proceedings**, Elsevier, v. 27, p. 2096–2100, 2020.

REICHARDT, A.; SHAPIRO, A. A.; OTIS, R.; DILLON, R. P.; BORGONIA, J. P.; MCENERNEY, B. W.; HOSEMANN, P.; BEESE, A. M. Advances in additive manufacturing of metal-based functionally graded materials. **International Materials Reviews**, Taylor & Francis, v. 66, n. 1, p. 1–29, 2021.

RUDY, E. A high temperature phase with the ζ-carbide structure in the molybdenum-chromium-carbon system. **Journal of the Less Common Metals**, Elsevier, v. 33, n. 3, p. 327–332, 1973.

SAILER, R.; MCCARTHY, G. Jcpds 44-1294. **The International Centre for Diffraction Data: Newtown Square, PA, USA**, 1993.

SASIKUMAR, Y.; INDIRA, K.; RAJENDRAN, N. Surface modification methods for titanium and its alloys and their corrosion behavior in biological environment: a review. **Journal of Bio-and Tribo-Corrosion**, Springer, v. 5, p. 1–25, 2019.

SCHREINER, W. Intelligent controls. **Inc., Amawalk. NY**, 1989.

SEMAK, V.; MATSUNAWA, A. The role of recoil pressure in energy balance during laser materials processing. **Journal of physics D: Applied physics**, IOP Publishing, v. 30, n. 18, p. 2541, 1997.

SHANG, C.; WANG, C.; XU, G.; LI, C.; YANG, G.; YOU, J. Dissimilar jointing of ta15 to inconel718 by laser additive manufacturing using nb/cu bilayer. **Journal of Manufacturing Processes**, Elsevier, v. 55, p. 153–160, 2020.

SMITH, T. M.; KANTZOS, C. A.; ZARKEVICH, N. A.; HARDER, B. J.; HECZKO, M.; GRADL, P. R.; THOMPSON, A. C.; MILLS, M. J.; GABB, T. P.; LAWSON, J. W. A 3d printable alloy designed for extreme environments. **Nature**, Nature Publishing Group UK London, p. 1–6, 2023.

STEEN, W. M.; MAZUMDER, J. **Laser material processing**. [S.l.]: springer science & business media, 2010.

SWANSON, H.; FUYAT, R.; UGRINIC, G. National bureau of standards circular 539. **Vol. II**, v. 23, 1953.

SZYMLEK, K. Review of titanium and steel welding methods. **Advances in materials science**, v. 8, n. 1, p. 186–194, 2008.

TESTING, A. S. for; MATERIALS (FILADELFIA, P. Astm e3-01: Standard guide for preparation of metallographic specimens. 2009.

TESTING, A. S. for; MATERIALS. Astm e384: standard test method for microindentation hardness of materials. In: ASTM WEST CONSHOHOCKEN. [S.l.], 2017.

THOMAS, J.; MOGONYE, J.; MANTRI, S.; CHOUDHURI, D.; BANERJEE, R.; SCHARF, T. Additive manufacturing of compositionally graded laser deposited titanium-chromium alloys. **Additive Manufacturing**, Elsevier, v. 33, p. 101132, 2020.

VEIGA, C.; DAVIM, J.; LOUREIRO, A. Properties and applications of titanium alloys: a brief review. **Rev. Adv. Mater. Sci**, v. 32, n. 2, p. 133–148, 2012.

VENKATRAMAN, M.; NEUMANN, J. The cr- mo (chromium-molybdenum) system. **Bulletin of Alloy Phase Diagrams**, Springer, v. 8, n. 3, p. 216–220, 1987.

VANDER VOORT, G. F.; LAMPMAN, S. R.; SANDERS, B. R.; ANTON, G. J.; POLAKOWSKI, C.; KINSON, J.; MULDOON, K.; HENRY, S. D.; SCOTT JR, W. W. Asm handbook. **Metallography and microstructures**, ASM International Materials Park, OH, v. 9, p. 44073–0002, 2004.

WYCKOFF, R. Hexagonal closest packed, hcp, structure. **Cryst. Struct**, Interscience Publishers New York, New York, v. 1, p. 7–83, 1963.

XU, P.-q.; LI, L.; ZHANG, C. S. Microstructure characterization of laser welded ti-6al-4v fusion zones. **Materials characterization**, Elsevier, v. 87, p. 179–185, 2014.

ZAGADE, P.; GAUTHAM, B.; DE, A.; DEBROY, T. Analytical estimation of fusion zone dimensions and cooling rates in part scale laser powder bed fusion. **Additive Manufacturing**, Elsevier, v. 46, p. 102222, 2021.

ZHANG, L.-C.; LIU, Y.; LI, S.; HAO, Y. Additive manufacturing of titanium alloys by electron beam melting: a review. **Advanced Engineering Materials**, Wiley Online Library, v. 20, n. 5, p. 1700842, 2018.